Supplementary Information

Selective electrosynthesis of 1,3-butadiene by tailoring the coverage of acetylene and water

Cheng *et al*.

1. Supplementary experimental section

Materials

Cu nanoparticles (10−30 nm, 99.9%, Meryer (Shanghai) Biochemical Technology Co., Ltd.), deuterium oxide (99.9%, Aladdin Co., Ltd.), KOH (95%, Aladdin Co., Ltd.), NaOH (99%, Aladdin Co., Ltd.), $(NH_4)_2S_2O_8$ (99%, Aladdin Co., Ltd.), Cu mesh (99.95%), ethanol (99.99%, Aladdin Co., Ltd.), ethanethiol (liquid, 98%, Aladdin Co., Ltd.), 1-hexanethiol (liquid, 96%, Aladdin Co., Ltd.), 1-decanethiol (liquid, 96%, Aladdin Co., Ltd.), 1-dodecanethiol (liquid, 98%, Aladdin Co., Ltd.), 1-tetradecanethiol (liquid, 97%, Aladdin Co., Ltd.), and 1-hexadecanethiol (solid, 97%, Aladdin Co., Ltd.). Rhodamine B (99.7%, Aladdin Co., Ltd.), gas diffusion layer carbon paper (GDL-CP, 28BC), proton exchange membranes (Nafion 117), and anion exchange membranes (FAA-3-PK-130) were purchased from Suzhou Sinero Technology Co., Ltd. Ar and pure acetylene gas were purchased from Tianjin Taiya Gas Sales Co., Ltd. All the chemicals used were of analytical grade and were used without further purification. Aqueous solutions were prepared by using ultrapure water (18.2 MΩ.cm).

Materials characterisation

Powder X-ray diffraction (XRD) was performed on a Bruker D8 Focus Diffraction System (Germany) using a Cu *K*α radiation source (λ = 0.154178 nm). Scanning electron microscopy (SEM) and energy dispersive spectroscopy (EDS) were conducted with an FEI Apreo S LoVac microscope (10 kV). The Raman spectra were obtained with a Renishaw inVia reflex Raman microscope under excitation with a 532 nm laser and a 633 nm laser at a power of 20 mW. Fourier transform infrared spectroscopy (FTIR) was performed on a Nicolet IS50 instrument with an MCT/A detector. The fluorescence spectra were obtained with a Nikon A1R+ microscope. The contact angles were measured via a Powereach JC2000C1 contact angle system (Shanghai Zhongchen Digital Technology Apparatus Co., Ltd.) at ambient temperature.

Synthesis of the Cu nanoarrays (denoted as Cu NAs)

The Cu meshes were ultrasonicated successively with acetone and diluted with hydrochloric acid for 15 minutes and then with ethanol for 5 minutes 3 times. In accordance with the literature[1], the pretreated Cu meshes were immersed in a mixture of aqueous solutions of 2.5 M NaOH and 0.13 M

$(NH_4)_2S_2O_8$ for 10 min. Cu NAs with a typical diameter of ca. 200 nm grew on the Cu meshes. The obtained Cu NAs were then removed and washed several times with ultrapure water. Finally, the Cu NAs were dried in a 60 ℃ vacuum drying oven overnight.

Synthesis of the thiol-modified Cu nanoarrays (denoted as Cu-xSH-NAs, where x represents the number of carbon atoms in the alkyl chain)

The Cu NAs were submerged in a 10 mM thiol ethanol solution for 1 min to form a thiol layer. The obtained Cu-xSH-NAs were then removed and washed several times with ethanol. Finally, the Cu-xSH-NAs were dried in a 60 ℃ vacuum drying oven overnight.

Fabrication of commercial Cu nanoparticles (denoted as Cu NPs)

Commercial Cu NPs were fabricated via the traditional spin-casting method. Commercial GDL-CP was cut into a square shape with a size of $2.5 \times 2.5\ cm^2$ as the electrode substrate. Specifically, 2 mg of Cu NPs were dissolved in 1 mL of ethanol with sonication for 1 h. Then, 4 μL of Nafion solution (5 wt%) was added to the solution with sonication for another 30 min. The as-prepared solution was then spin-coated on the GDL-CP substrates with 1 mL on each substrate under a constant spin speed of 500 rpm.

Quantitative analysis of the C_2H_2 conversion, evolution rate, and FEs of the obtained products

The products were subjected to an Agilent 7890A gas chromatograph equipped with columns, including plot-Q and 5A molecular sieves; two detectors, a flame ionization detector (FID) and a thermal conductivity detector (TCD); and He as the carrier gas. The evolution rates of the different products were calculated via Eqs. S1−S3 and the FEs of the different products were calculated via Eq. S4. All the experiments with error bars were repeated three times.

$$c_X = pk_X \quad (S1)$$

$$n_X = c_X S t \quad (S2)$$

$$\text{Evolution Rate (mmol mg}^{-1}\text{ h}^{-1}) = c_X S/m \quad (S3)$$

$$FE_X\ (\%) = aFn_X/Q \quad (S4)$$

X: The feedstock and products, including H_2, C_2H_2, C_2H_4, C_2H_6, C_4H_6, and C_4H_8 (including 1-C_4H_8, (Z)-2-C_4H_8, and (E)-2-C_4H_8).

p: Peak area of feedstock and products.

t: The continuous time of electrocatalytic C_2H_2 hydrogenation (EAH).

c: Concentrations of feedstock and products.

m: The mass of the catalyst over the electrode.

n: moles of feedstock and products.

k: The slope of the calibration curves for feedstock and products.

S: The gas flow rate.

a: Electron transfer number.

F: Faraday constant.

Q: The total Coulomb number of the EAH.

2. Supplementary computational section

Supplementary Note 1. Computational details

All the DFT calculations were performed via the Vienna ab initio simulation package (VASP)[2]. The projector augmented wave (PAW) pseudopotential with the PBE generalized gradient approximation (GGA) exchange-correlation function was utilized in the computations[3,4]. The cut-off energy of the plane wave basis set was 500 eV, and a Monkhorst-Pack mesh of 3×3×1 was used in K-sampling for the adsorption energy calculations and other nonself-consistent calculations. The long-range dispersion interaction was described via the DFT-D3 method. The electrolyte was incorporated implicitly with the Poisson–Boltzmann model implemented in VASPsol[5]. The relative permittivity of the media was chosen to be $\epsilon_r = 78.4$, corresponding to that of water. All the atoms were fully relaxed with an energy convergence tolerance of 10^{-5} eV per atom, and the final force on each atom was < 0.05 eV $Å^{-1}$.

The transition state (TS) searches were performed via the Dimer method in the VTST package. The final force on each atom was < 0.1 eV $Å^{-1}$. The TS search is conducted by using the climbing-image nudged elastic band (CI-NEB) method to generate initial guess geometries, followed by the dimer method to converge to the saddle points.

For the ab initio molecular dynamics (AIMD) simulations, canonical ensemble (NVT) conditions were imposed by a Nose–Hoover thermostat with a target temperature of 300 K. The MD time step was 1 fs, and all the systems were run for 10 ps to reach equilibrium. Three different alkanethiol molecules with 2, 6, and 12 carbon atoms were introduced to the copper surface to simulate the dynamic behavior of interfacial water with increasing ligand length at an approximately 1 g/cm^3 water density. The last 1 ps of data in the AIMD process are selected for analysis. In the process of hydrogen bond analysis, we set the maximum distance of the hydrogen bond to 2.6 Å.

The adsorption energy of the reaction intermediates can be computed via Eqs. S5−S6:

$$\Delta E = E_{*\mathrm{ads}} - (E_{*} + E_{\mathrm{ads}}) \qquad \text{(S5)}$$

$$\Delta G = \Delta E + \Delta E_{\mathrm{ZPE}} - T\Delta S \qquad \text{(S6)}$$

where ΔE_{ZPE} is the zero-point energy change and ΔS is the entropy change. In this work, the values of ΔE_{ZPE} and ΔS were obtained via vibration frequency calculations.

Supplementary Note 2. The rate expressions

For an electrochemical reaction (Eq. S7), the full Butler−Volmer equation (Eq. S8) can be simplified to Eq. S9 only if the overpotential is sufficiently high that the rate of the reverse reaction is negligible compared with that of the forward reaction[6].

$$O_x + ne^- \rightarrow R_{ed} \quad \text{(S7)}$$

$$j = nFk_b^0 a[R_{ed}]\exp[(1-\alpha)f\eta] - nFk_f^0 a[O_x]\exp[-\alpha f\eta] \quad \text{(S8)}$$

$$j = -nFk_f^0 a[O_x]\exp(-\alpha f\eta) \quad \text{(S9)}$$

In these equations, j is the current density; η is the overpotential for the cathodic reaction; k_f^0 is the standard forward rate constant; k_b^0 is the standard backwards rate constant; F is the Faraday constant; $f = F/RT$, where R is the ideal gas constant and T is the absolute temperature; α is the transfer coefficient assumed to be equal to 0.5; n is the number of transferred electrons; and $a[R_{ed}]$ and $a[O_x]$ are the concentrations of reductant and oxidant, respectively.

Under equilibrium conditions ($j = 0$), Eq. S8 can be simplified to Eq. S10, and then, from a brief deformation, Eq. S11 can be obtained.

$$nFk_b^0 a[R_{ed}]\exp[(1-\alpha)f\eta] = nFk_f^0 a[O_x]\exp[-\alpha f\eta] \quad \text{(S10)}$$

$$a[R_{ed}]/a[O_x] = K^\theta \exp(-f\eta) \quad \text{(S11)}$$

In these equations, $K^\theta = k_f^0/k_b^0$ is the standard equilibrium constant where T = 25 ℃.

Under alkaline conditions, H_2O is considered a proton donor. The proposed reaction mechanism is written below (Eqs. S12−S21), and the expected rate expression can be derived as a function of the reaction intermediates, assuming that one of the processes is the possible rate-determining step (RDS):

A $$C_2H_2 + * \rightarrow *C_2H_2 \quad \text{(S12)}$$

B $$*C_2H_2 + H_2O + e^- \rightarrow *C_2H_3 + OH^- \quad \text{(S13)}$$

C $$*C_2H_3 + H_2O + e^- \rightarrow *C_2H_4 + OH^- \quad \text{(S14)}$$

D $$*C_2H_4 \rightarrow C_2H_4 + * \quad \text{(S15)}$$

E1 $$*C_2H_2 + *C_2H_2 \rightarrow *C_4H_4 + * \quad \text{(S16)}$$

E2 $$*C_2H_3 + *C_2H_2 \rightarrow *C_4H_5 + * \quad \text{(S17)}$$

E3 $$*C_2H_3 + *C_2H_3 \rightarrow *C_4H_6 + * \quad (S18)$$

F $$*C_4H_4 + H_2O + e^- \rightarrow *C_4H_5 + OH^- \quad (S19)$$

G $$*C_4H_5 + H_2O + e^- \rightarrow *C_4H_6 + OH^- \quad (S20)$$

H $$*C_4H_6 \rightarrow C_4H_6 + * \quad (S21)$$

Since the calculated energy barriers of coupling are all higher than those of hydrogenation for all three paths (Figs. 1b, c), the three different coupling steps are assumed to constitute the RDS for the following derivation.

If Eq. S16 (C−H pathway) is assumed to be the RDS, according to Eq. S9 and Eq. S11, the following rate expression can be deduced:

$$j_{C4H6} = 2Fk^0_{E1}a^2[*C_2H_2]$$

$$K^\theta_A = a[*C_2H_2]/(a[C_2H_2]\theta^*)$$

$$\Rightarrow a[*C_2H_2] = K^\theta_A a[C_2H_2]\theta^*$$

$$\Rightarrow j_{C4H6} = 2FK^\theta_A k^0_{E1}a^2[C_2H_2](\theta^*)^2$$

If Eq. S17 (H−C−1 pathway) is assumed to be the RDS, according to Eq. S9 and Eq. S11, the following rate expression can be deduced:

$$j_{C4H6} = 2Fk^0_{E2}a[*C_2H_2]a[*C_2H_3]$$

$$K^\theta_B\exp(-f\eta) = a[*C_2H_3]a[OH^-]/(a[*C_2H_2]a[H_2O])$$

$$\Rightarrow a[*C_2H_3] = K^\theta_B a[*C_2H_2]a[H_2O]\exp(-f\eta)/a[OH^-]$$

$$\Rightarrow a[*C_2H_3] = K^\theta_B a[*C_2H_2]a[H_2O]a[H^+]\exp(-f\eta)/K_W$$

$$K^\theta_A = a[*C_2H_2]/(a[C_2H_2]\theta^*)$$

$$\Rightarrow a[*C_2H_2] = K^\theta_A a[C_2H_2]\theta^*$$

$$\Rightarrow j_{C4H6} = 2F(K^\theta_A)^2K^\theta_B k^0_{E2}a[H_2O]a[H^+]a^2[C_2H_2](\theta^*)^2\exp(-f\eta)/K_W$$

If Eq. S18 (H−C−2 pathway) is assumed to be the RDS, according to Eq. S9 and Eq. S11, the following rate expression can be deduced:

$$j_{C4H6} = 2Fk^0_{E3}a^2[*C_2H_3]$$

$$K^\theta_B\exp(-f\eta) = a[*C_2H_3]a[OH^-]/(a[*C_2H_2]a[H_2O])$$

$$\Rightarrow a[*C_2H_3] = K^\theta_B a[*C_2H_2]a[H_2O]\exp(-f\eta)/a[OH^-]$$

$$\Rightarrow a[*C_2H_3] = K^\theta_B a[*C_2H_2]a[H_2O]a[H^+]\exp(-f\eta)/K_W$$

$$K^\theta_A = a[*C_2H_2]/(a[C_2H_2]\theta^*)$$

$$\Rightarrow a[{*}C_2H_2] = K_A^{\theta} a[C_2H_2]\theta^{*}$$

$$\Rightarrow j_{C4H6} = 2F(K_A^{\theta}K_B^{\theta})^2 k_{E3}^{0} a^2[H_2O]a^2[H^+]a^2[C_2H_2](\theta^{*})^2\exp(-2f\eta)/K_W{}^2$$

In addition, an important subtlety should be noted when product desorption is assumed to be the RDS because this step itself does not involve H_2O. However, the rate expressions are still related to H_2O/H^+ as follows:

If Eqn. S21 is assumed to be the RDS, according to Eq. S9 and Eq. S11, the following rate expression can be deduced:

(1) A-E1-F-G-H process:

$$j_{C4H6} = 2Fk_H^{0} a[{*}C_4H_6]$$

$$K_G^{\theta}\exp(-f\eta) = a[{*}C_4H_6]a[OH^-]/(a[{*}C_4H_5]a[H_2O])$$

$$\Rightarrow a[{*}C_4H_6] = K_G^{\theta} a[{*}C_4H_5]a[H_2O]\exp(-f\eta)/a[OH^-]$$

$$\Rightarrow a[{*}C_4H_6] = K_G^{\theta} a[{*}C_4H_5]a[H_2O]a[H^+]\exp(-f\eta)/K_W$$

$$K_F^{\theta}\exp(-f\eta) = a[{*}C_4H_5]a[OH^-]/(a[{*}C_4H_4]a[H_2O])$$

$$\Rightarrow a[{*}C_4H_5] = K_F^{\theta} a[{*}C_4H_4]a[H_2O]\exp(-f\eta)/a[OH^-]$$

$$\Rightarrow a[{*}C_4H_5] = K_F^{\theta} a[{*}C_4H_4]a[H_2O]a[H^+]\exp(-f\eta)/K_W$$

$$K_{E1}^{\theta} = a[{*}C_4H_4]\theta^{*}/a^2[{*}C_2H_2]$$

$$\Rightarrow a[{*}C_4H_4] = K_{E1}^{\theta} a^2[{*}C_2H_2]/\theta^{*}$$

$$K_A^{\theta} = a[{*}C_2H_2]/(a[C_2H_2]\theta^{*})$$

$$\Rightarrow a[{*}C_2H_2] = K_A^{\theta} a[C_2H_2]\theta^{*}$$

$$j_{C4H6} = 2F(K_A^{\theta})^2 K_{E1}^{\theta} K_F^{\theta} K_G^{\theta} k_H^{0} a^2[C_2H_2]a^2[H_2O]a^2[H^+]\theta^{*}\exp(-2f\eta)/K_W{}^2$$

(2) A-B-E2-G-H process:

$$j_{C4H6} = 2Fk_H^{0} a[{*}C_4H_6]$$

$$K_G^{\theta}\exp(-f\eta) = a[{*}C_4H_6]a[OH^-]/(a[{*}C_4H_5]a[H_2O])$$

$$\Rightarrow a[{*}C_4H_6] = K_G^{\theta} a[{*}C_4H_5]a[H_2O]\exp(-f\eta)/a[OH^-]$$

$$\Rightarrow a[{*}C_4H_6] = K_G^{\theta} a[{*}C_4H_5]a[H_2O]a[H^+]\exp(-f\eta)/K_W$$

$$K_{E2}^{\theta} = a[{*}C_4H_5]\theta^{*}/(a[{*}C_2H_2]a[{*}C_2H_3])$$

$$\Rightarrow a[{*}C_4H_5] = K_{E2}^{\theta} a[{*}C_2H_2]a[{*}C_2H_3]/\theta^{*}$$

$$K_B^{\theta}\exp(-f\eta) = a[{*}C_2H_3]a[OH^-]/(a[{*}C_2H_2]a[H_2O])$$

$$\Rightarrow a[{*}C_2H_3] = K_B^{\theta} a[{*}C_2H_2]a[H_2O]\exp(-f\eta)/a[OH^-]$$

$$\Rightarrow a[{*}C_2H_3] = K_B^{\theta} a[{*}C_2H_2] a[H_2O] a[H^+] \exp(-f\eta)/K_W$$

$$K_A^{\theta} = a[{*}C_2H_2]/(a[C_2H_2]\theta^*)$$

$$\Rightarrow a[{*}C_2H_2] = K_A^{\theta} a[C_2H_2]\theta^*$$

$$j_{C4H6} = 2F(K_A^{\theta})^2 K_B^{\theta} K_{E2}^{\theta} K_G^{\theta} k_H^0 a^2[C_2H_2] a^2[H_2O] a^2[H^+]\theta^* \exp(-2f\eta)/K_W{}^2$$

(3) A-B-E3-H process:

$$j_{C4H6} = 2Fk_H^0 a[{*}C_4H_6]$$

$$K_{E3}^{\theta} = a[{*}C_4H_6]\theta^*/a^2[{*}C_2H_3]$$

$$\Rightarrow a[{*}C_4H_6] = K_{E3}^{\theta} a^2[{*}C_2H_3]/\theta^*$$

$$K_B^{\theta} \exp(-f\eta) = a[{*}C_2H_3] a[OH^-]/(a[{*}C_2H_2] a[H_2O])$$

$$\Rightarrow a[{*}C_2H_3] = K_B^{\theta} a[{*}C_2H_2] a[H_2O] \exp(-f\eta)/a[OH^-]$$

$$\Rightarrow a[{*}C_2H_3] = K_B^{\theta} a[{*}C_2H_2] a[H_2O] a[H^+] \exp(-f\eta)/K_W$$

$$K_A^{\theta} = a[{*}C_2H_2]/(a[C_2H_2]\theta^*)$$

$$\Rightarrow a[{*}C_2H_2] = K_A^{\theta} a[C_2H_2]\theta^*$$

$$j_{C4H6} = 2F(K_A^{\theta} K_B^{\theta})^2 K_{E3}^{\theta} k_H^0 a^2[C_2H_2] a^2[H^+] a^2[H_2O]\theta^* \exp(-2f\eta)/K_W{}^2$$

Therefore, the specific coupling path and RDS of electrocatalytic acetylene dimeric hydrogenation to C_4H_6 can be determined by comparing the theoretical rate expression to the experimental reaction order of H_2O/H^+. The latter could be clarified through pH dependency and kinetic isotope effect (KIE) experiments[7,8].

Supplementary model structure information

Fractional coordinates for periodic Cu slabs in the DFT calculation

a	b	c	alpha	beta	gamma
12.64810	12.64810	25.00000	90.0000	90.0000	120.0000

Unit-cell volume = 3463.548031 Å^3

Structure parameters

		x	y	z
1 Cu	Cu1	0.00154	0.99957	0.33357
2 Cu	Cu2	0.00377	0.40218	0.33314
3 Cu	Cu3	0.60006	0.79697	0.32529
4 Cu	Cu4	0.59951	0.39881	0.32495
5 Cu	Cu5	0.39740	0.79440	0.33202
6 Cu	Cu6	0.00311	0.60004	0.33419
7 Cu	Cu7	0.59846	0.99770	0.33011
8 Cu	Cu8	0.39911	0.39880	0.32506
9 Cu	Cu9	0.00150	0.19995	0.33201
10 Cu	Cu10	0.39876	0.19749	0.32659
11 Cu	Cu11	0.39863	0.99784	0.33190
12 Cu	Cu12	0.19786	0.80055	0.32810
13 Cu	Cu13	0.20308	0.40025	0.32849
14 Cu	Cu14	0.39913	0.59839	0.32296
15 Cu	Cu15	0.20012	0.00021	0.33549

16	Cu	Cu16	0.99869	0.79894	0.33401
17	Cu	Cu17	0.80096	0.20043	0.33101
18	Cu	Cu18	0.80325	0.60015	0.32549
19	Cu	Cu19	0.20338	0.20339	0.33574
20	Cu	Cu20	0.79971	0.99856	0.33136
21	Cu	Cu21	0.19976	0.59897	0.32482
22	Cu	Cu22	0.79718	0.79663	0.33230
23	Cu	Cu23	0.79827	0.39993	0.33264
24	Cu	Cu24	0.59929	0.20136	0.33264
25	Cu	Cu25	0.59719	0.59516	0.33160
26	Cu	Cu26	0.73523	0.66724	0.24475
27	Cu	Cu27	0.73365	0.26624	0.24550
28	Cu	Cu28	0.73605	0.86792	0.24360
29	Cu	Cu29	0.33274	0.66760	0.24457
30	Cu	Cu30	0.73581	0.46682	0.24339
31	Cu	Cu31	0.13173	0.26331	0.24515
32	Cu	Cu32	0.73397	0.06656	0.24483
33	Cu	Cu33	0.93600	0.66767	0.24441
34	Cu	Cu34	0.13196	0.66699	0.24417
35	Cu	Cu35	0.53548	0.66753	0.24319
36	Cu	Cu36	0.33120	0.26277	0.24397
37	Cu	Cu37	0.33297	0.86671	0.24591

38 Cu	Cu38	0.93293	0.26499	0.24575
39 Cu	Cu39	0.33049	0.46363	0.24234
40 Cu	Cu40	0.53224	0.26359	0.24350
41 Cu	Cu41	0.33199	0.06367	0.24461
42 Cu	Cu42	0.13227	0.86739	0.24556
43 Cu	Cu43	0.13080	0.46299	0.24406
44 Cu	Cu44	0.53363	0.06670	0.24539
45 Cu	Cu45	0.53421	0.46691	0.24523
46 Cu	Cu46	0.53424	0.86754	0.24465
47 Cu	Cu47	0.93357	0.06566	0.24583
48 Cu	Cu48	0.13331	0.06571	0.24716
49 Cu	Cu49	0.93373	0.46604	0.24639
50 Cu	Cu50	0.93376	0.86656	0.24651
51 Cu	Cu51	0.06648	0.53295	0.16253
52 Cu	Cu52	0.06689	0.13246	0.16265
53 Cu	Cu53	0.06678	0.93380	0.16283
54 Cu	Cu54	0.86723	0.73381	0.16245
55 Cu	Cu55	0.86692	0.33295	0.16279
56 Cu	Cu56	0.46576	0.13247	0.16192
57 Cu	Cu57	0.46684	0.53235	0.16221
58 Cu	Cu58	0.06672	0.33221	0.16233
59 Cu	Cu59	0.46659	0.93358	0.16265

60 Cu	Cu60	0.06752	0.73442	0.16187
61 Cu	Cu61	0.66710	0.73331	0.16188
62 Cu	Cu62	0.46615	0.73293	0.16219
63 Cu	Cu63	0.66647	0.33265	0.16241
64 Cu	Cu64	0.46645	0.33303	0.16222
65 Cu	Cu65	0.86719	0.13283	0.16253
66 Cu	Cu66	0.86774	0.53387	0.16230
67 Cu	Cu67	0.86764	0.93355	0.16236
68 Cu	Cu68	0.26609	0.13229	0.16231
69 Cu	Cu69	0.26650	0.53386	0.16174
70 Cu	Cu70	0.26684	0.73334	0.16228
71 Cu	Cu71	0.26634	0.93203	0.16247
72 Cu	Cu72	0.26617	0.33245	0.16183
73 Cu	Cu73	0.66668	0.13305	0.16253
74 Cu	Cu74	0.66638	0.53296	0.16227
75 Cu	Cu75	0.66656	0.93327	0.16204
76 Cu	Cu76	0.00000	0.20000	0.08000
77 Cu	Cu77	0.20000	0.20000	0.08000
78 Cu	Cu78	0.20000	0.60000	0.08000
79 Cu	Cu79	0.60000	0.20000	0.08000
80 Cu	Cu80	0.60000	0.60000	0.08000
81 Cu	Cu81	0.20000	0.00000	0.08000

82	Cu	Cu82	0.20000	0.40000	0.08000
83	Cu	Cu83	0.20000	0.80000	0.08000
84	Cu	Cu84	0.60000	0.00000	0.08000
85	Cu	Cu85	0.60000	0.40000	0.08000
86	Cu	Cu86	0.60000	0.80000	0.08000
87	Cu	Cu87	0.00000	0.60000	0.08000
88	Cu	Cu88	0.40000	0.20000	0.08000
89	Cu	Cu89	0.80000	0.80000	0.08000
90	Cu	Cu90	0.40000	0.60000	0.08000
91	Cu	Cu91	0.80000	0.40000	0.08000
92	Cu	Cu92	0.80000	0.00000	0.08000
93	Cu	Cu93	0.80000	0.60000	0.08000
94	Cu	Cu94	0.80000	0.20000	0.08000
95	Cu	Cu95	0.40000	0.80000	0.08000
96	Cu	Cu96	0.40000	0.40000	0.08000
97	Cu	Cu97	0.40000	0.00000	0.08000
98	Cu	Cu98	0.00000	0.80000	0.08000
99	Cu	Cu99	0.00000	0.40000	0.08000
100	Cu	Cu100	0.00000	0.00000	0.08000
101	H	H1	0.51471	0.75008	0.43589
102	H	H2	0.23146	0.70977	0.43517
103	H	H3	0.70476	0.53892	0.43427

104 H	H4	0.41942	0.49333	0.43482
105 H	H5	0.66637	0.13154	0.36589
106 H	H6	0.26979	0.92606	0.36829
107 H	H7	0.28154	0.35192	0.36834
108 H	H8	0.65808	0.33897	0.36805
109 H	H9	0.65525	0.73067	0.36571
110 H	H10	0.06754	0.13460	0.36906
111 H	H11	0.08147	0.53885	0.36835
112 H	H12	0.07470	0.33762	0.36671
113 H	H13	0.06676	0.93049	0.37026
114 H	H14	0.07193	0.73199	0.36864
115 H	H15	0.85440	0.72178	0.36676
116 H	H16	0.27717	0.14231	0.36842
117 H	H17	0.86780	0.33406	0.36679
118 H	H18	0.46416	0.13755	0.36591
119 H	H19	0.46647	0.93217	0.36516
120 H	H20	0.65700	0.92305	0.36443
121 H	H21	0.86580	0.13126	0.36633
122 H	H22	0.86129	0.53416	0.36633
123 H	H23	0.86509	0.93067	0.36746
124 C	C1	0.42401	0.73613	0.43219
125 C	C2	0.32126	0.72140	0.43184

126 C	C3	0.61392	0.52479	0.43081
127 C	C4	0.51071	0.50900	0.43113

3. Supplementary details for Carbon emission life cycle assessment (LCA)

Supplementary Note 3. Carbon emission life cycle assessment

The electrocatalytic C_4H_6 synthesis strategy considered here involved the mining of coal, acetylene production from coal via the hydrogen plasmon method, and electrocatalytic acetylene coupling-hydrogenation at room temperature and ambient pressure. Note that the current LCA model was aimed at CO_2 emissions from the process of C_4H_6 production from coal. Since geographical considerations are key in the assumption of an LCA[9,10], the scope of the analysis of the mining and preparation of coal was based in China. Additionally, the parameters of acetylene production from coal were obtained from state-of-the-art pilot-scale production in China[11]. The carbon footprint of coal-to-acetylene conversion processes is negligible because of the operation of plasmonic acetylene production from coal, which does not lead to high CO_2 emissions[11]. According to the reported work[12], the emissions generated from the construction of the electrolyzer or the separation equipment were not considered, since these were expected to be far lower than the emissions from the operation, and electrical energy was the only energy requirement for the electrocatalytic acetylene coupling-hydrogenation part. In other words, the operation accounted for most of the CO_2 emissions in the C_4H_6 electrosynthesis process. Thus, the majority of emissions originate from coal mining and electricity generation.

The calculation of the CO_2 emissions is described below according to the reported literature:

Energy efficiency = $E°$ × FE/cell voltage

1. Energy for C_2H_2 coupling–hydrogenation = the energy density of C_4H_6/energy efficiency
2. The total CO_2 emissions = (Energy for C_2H_2 production + Energy for C_2H_2 coupling-hydrogenation + Energy for C_2H_2 separation) × Carbon intensity + CO_2 emissions from the mining of coal

All the constants of the model are provided in Supplementary Table 4.

The cradle-to-gate CO_2 emissions for C_4H_6 from the conventional naphtha cracking process were 2.5 kg CO_2e/kg C_4H_6, which were obtained from the previously reported literature[13]. The cradle-to-gate CO_2 emissions from the mining of coal in China were 0.121 kg CO_2e/kg coal, as taken from the SimaPro LCA database[14]. The energy for acetylene production from the plasmonic method and C_2H_2 separation was taken from state-of-the-art pilot-scale production in China. Note that the carbon

intensities were the CO_2 emissions per kWh of the generated electricity[9]. The 70% full-cell energy efficiency (EE) of the C_2H_2 semihydrogenation electrolyzer was set according to the reported literature[12,15].

4. Supplementary Figures

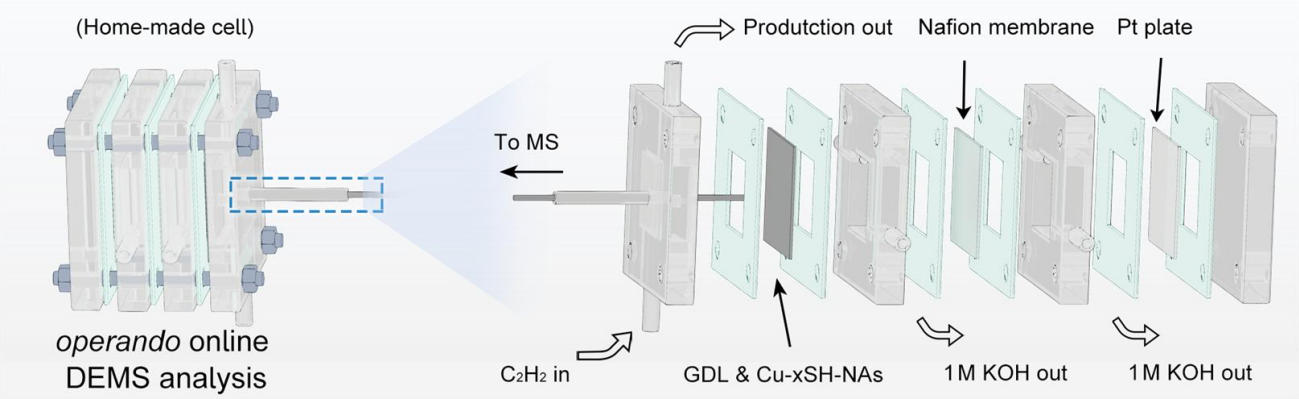

Supplementary Figure 1. Schematic illustration of the equipment applied in the online operando DEMS analysis.

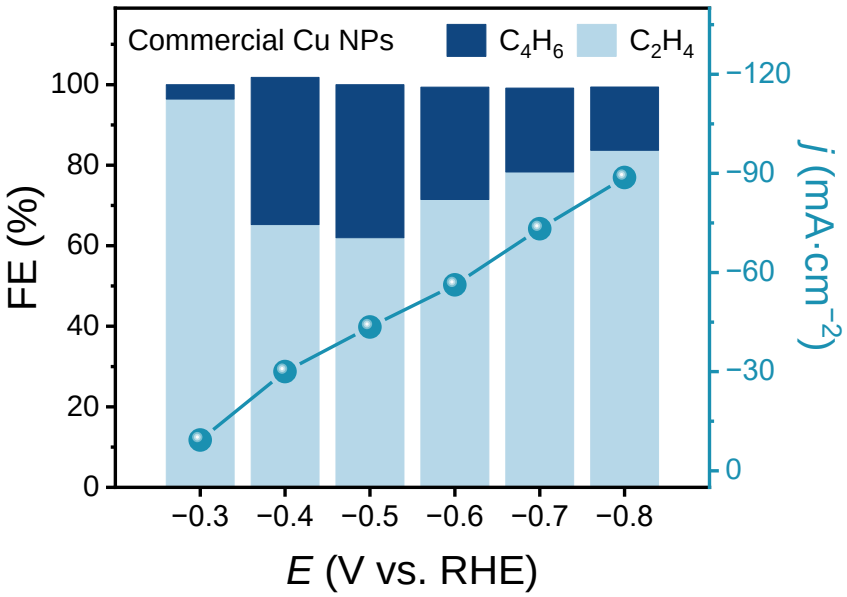

Supplementary Figure 2. FEs and current densities at different potentials in a 1 M KOH aqueous solution under pure C_2H_2 flow over the Cu NPs.

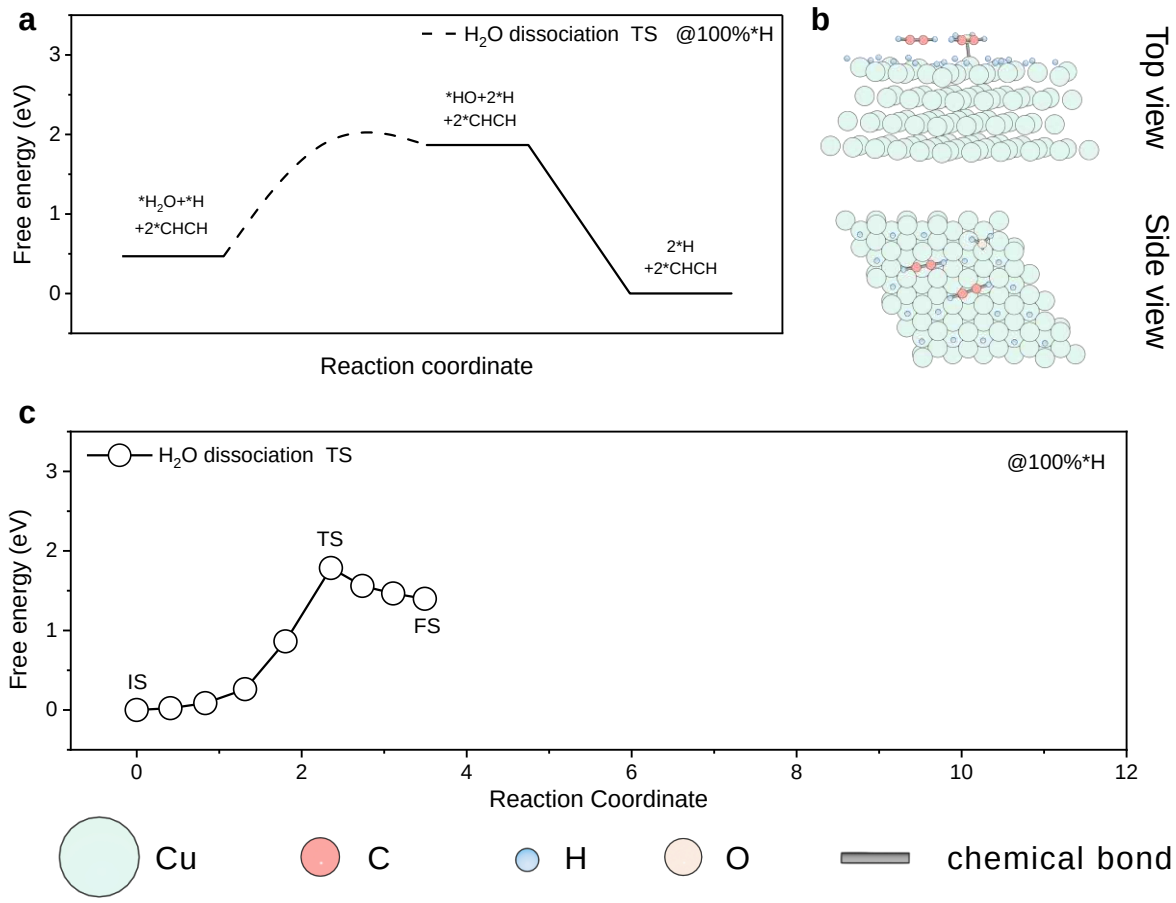

Supplementary Figure 3. Free energy diagram of the H_2O dissociation process over the Cu NPs (a), the optimized structures for theoretical calculations (b), and corresponding energy change profile (c). To simulate actual electrocatalytic hydrogenation using water as a hydrogen source in an alkaline electrolyte, the process of H_2O dissociation to H* was first calculated before considering the following C_2H_2 coupling and/or hydrogenation steps.

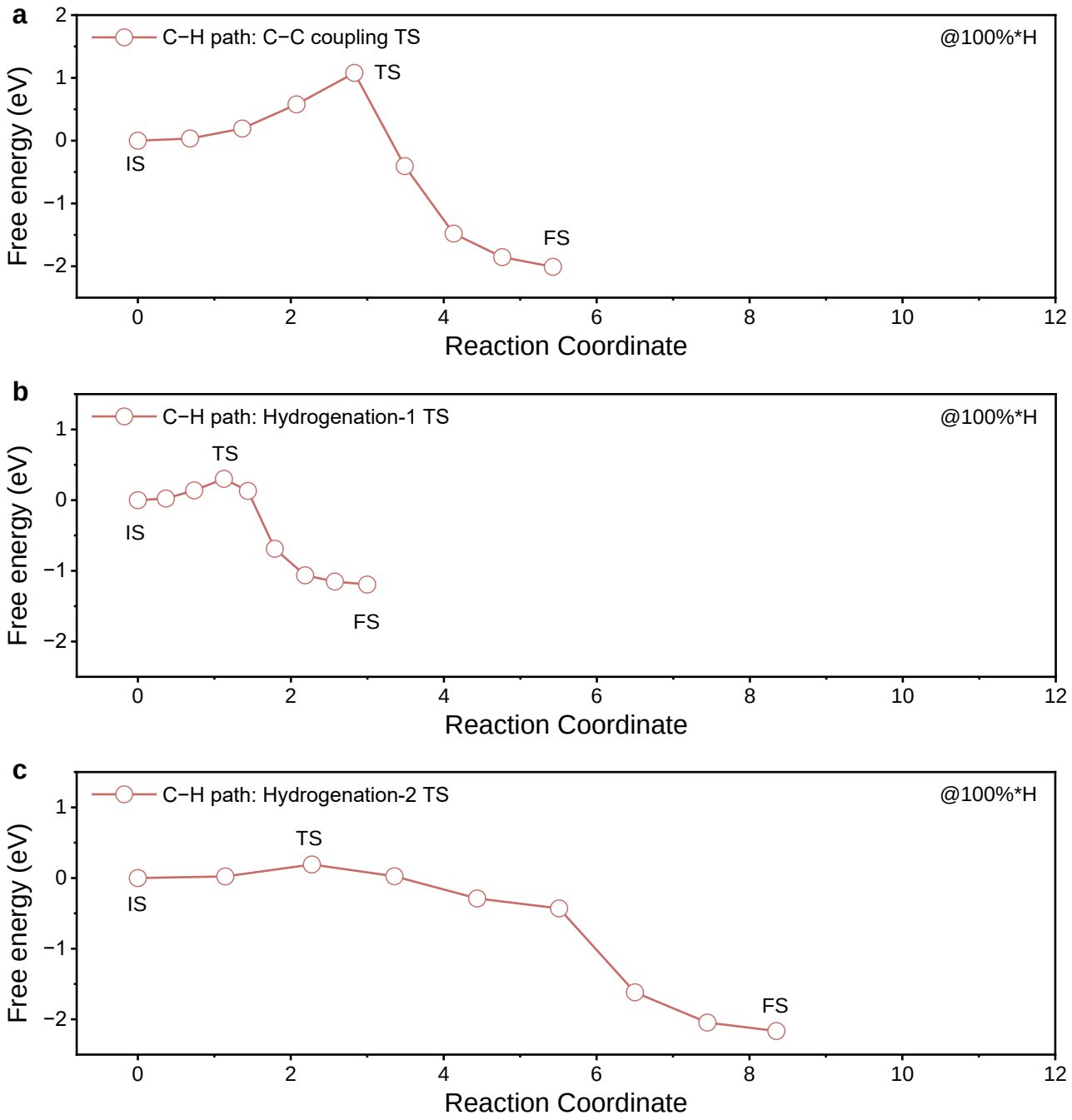

Supplementary Figure 4. Energy change profiles of the C_2H_2 dimeric hydrogenation process for the C−H path.

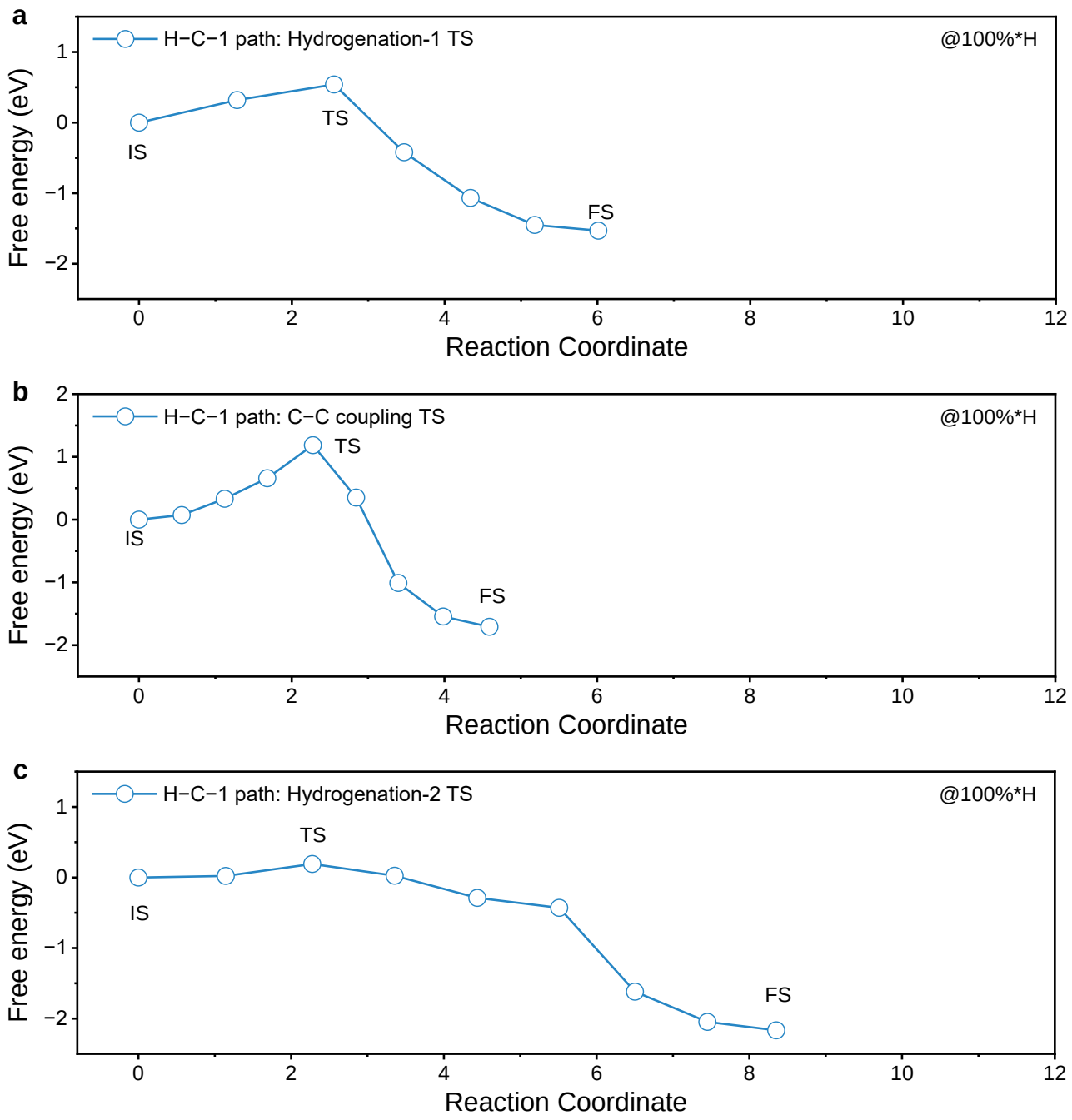

Supplementary Figure 5. Energy change profiles of the C_2H_2 dimeric hydrogenation process for the H−C−1 path.

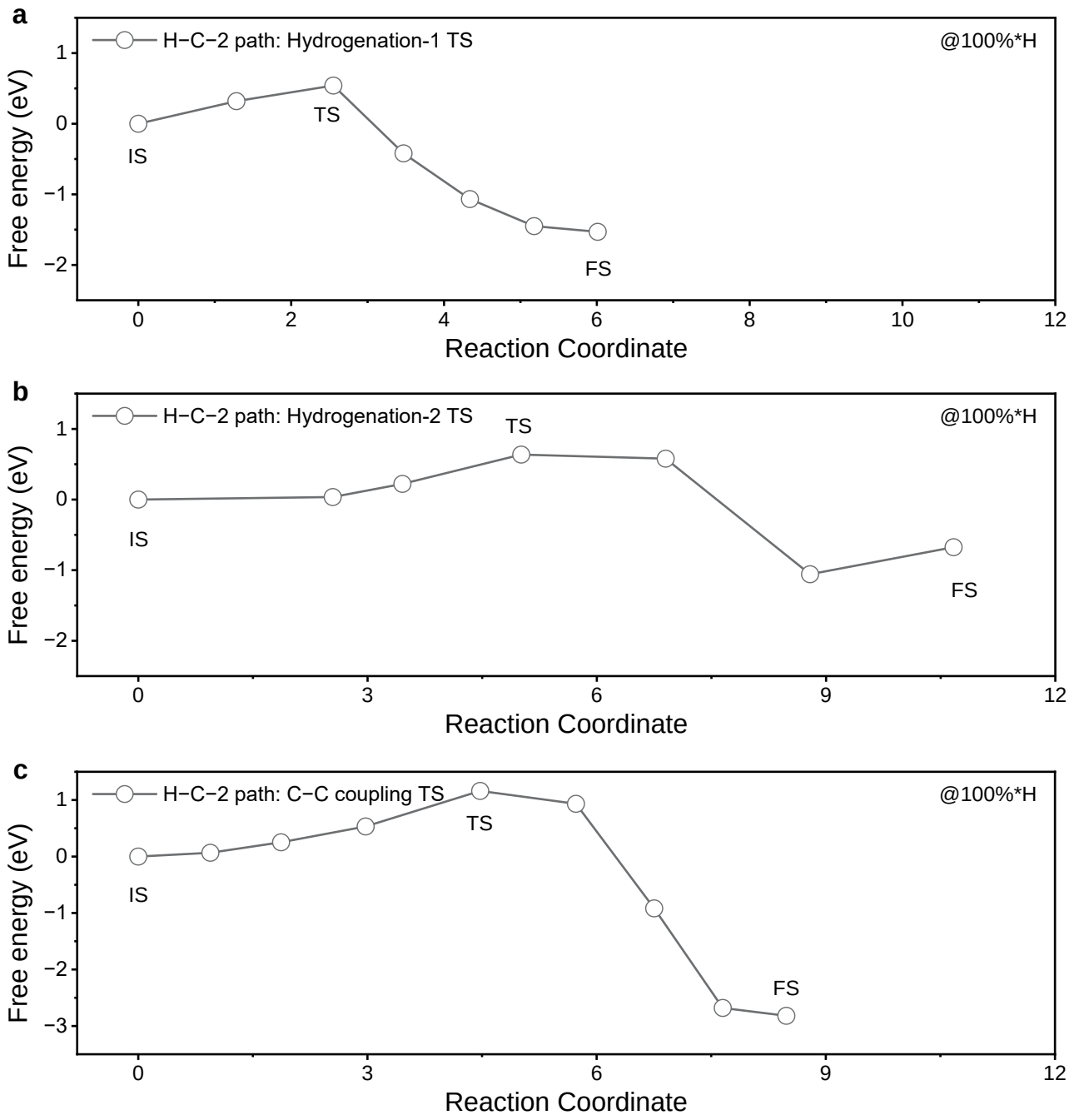

Supplementary Figure 6. Energy change profiles of the C_2H_2 dimeric hydrogenation process for the H−C−2 path.

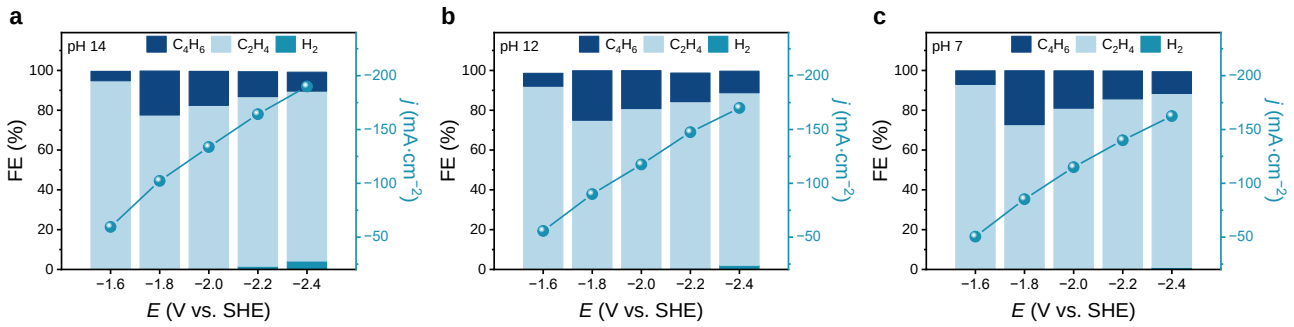

Supplementary Figure 7. FEs and current densities at different potentials over commercial Cu NPs in different solutions: 1 M KOH aqueous solution (a), 0.01 M KOH and 0.495 M K_2SO_4 aqueous solution (b), and 0.5 M K_2SO_4 aqueous solution (c).

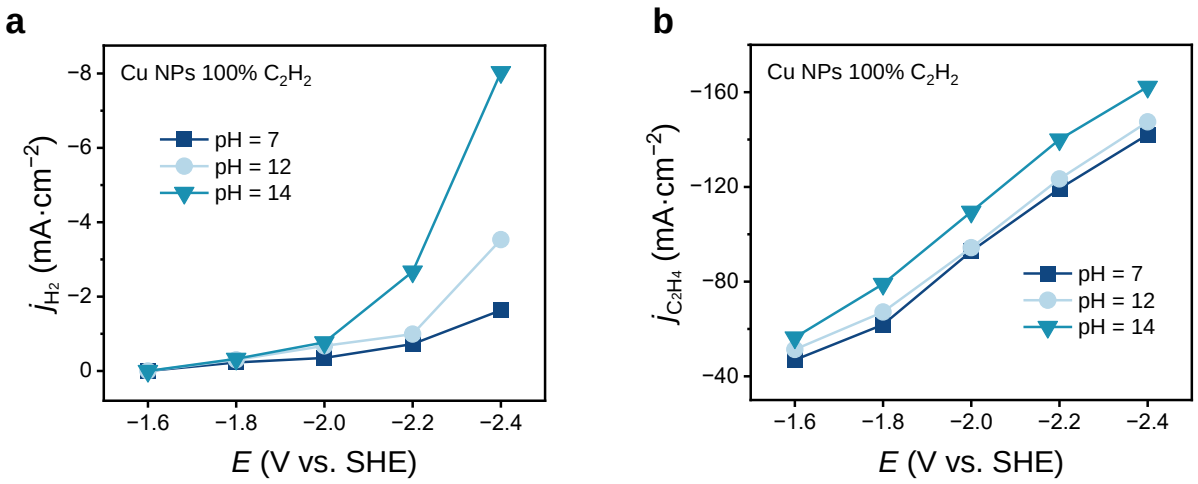

Supplementary Figure 8. Partial current densities of H_2 (a) and C_2H_4 (b) at different potentials over commercial Cu NPs with different pH values.

Unlike the almost unchanged $j_{C_4H_6}$ shown in Fig. 1e, the activity of the hydrogen evolution reaction and C_2H_4 production is obviously affected by the pH.

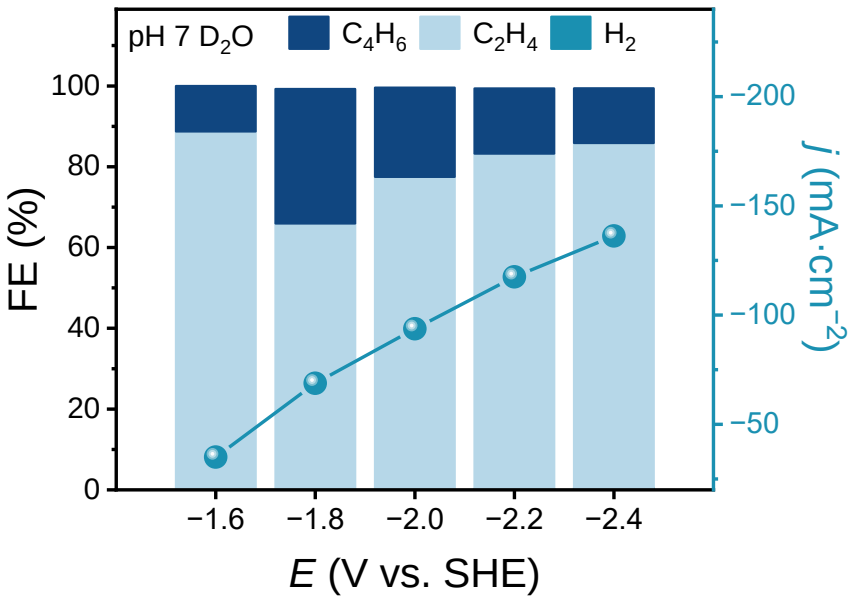

Supplementary Figure 9. FEs and current densities at different potentials over commercial Cu NPs in a 0.5 M K_2SO_4 aqueous solution.

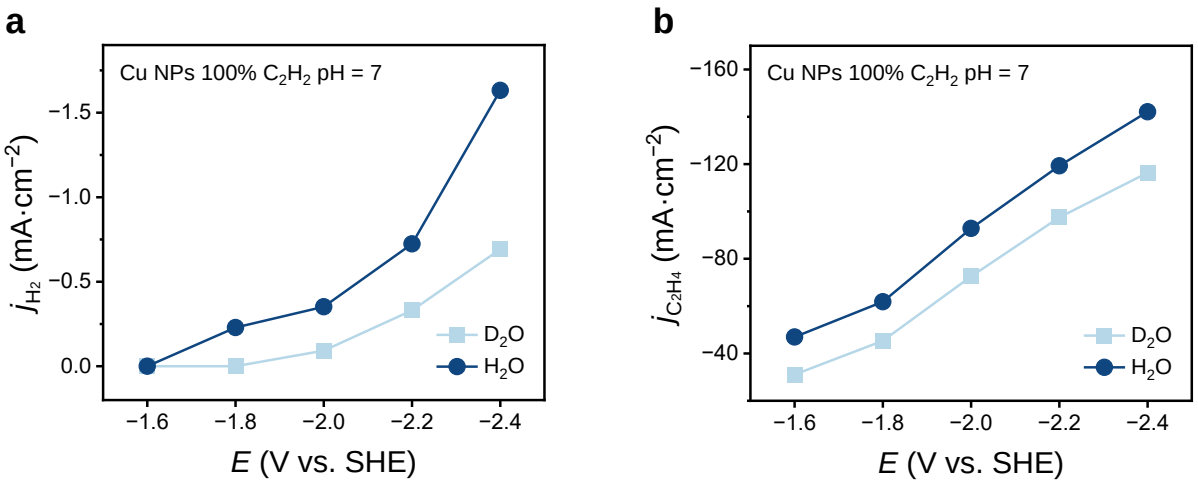

Supplementary Figure 10. Partial current densities of H_2 (a) and C_2H_4 (b) at different potentials over commercial Cu NPs with the same pH.

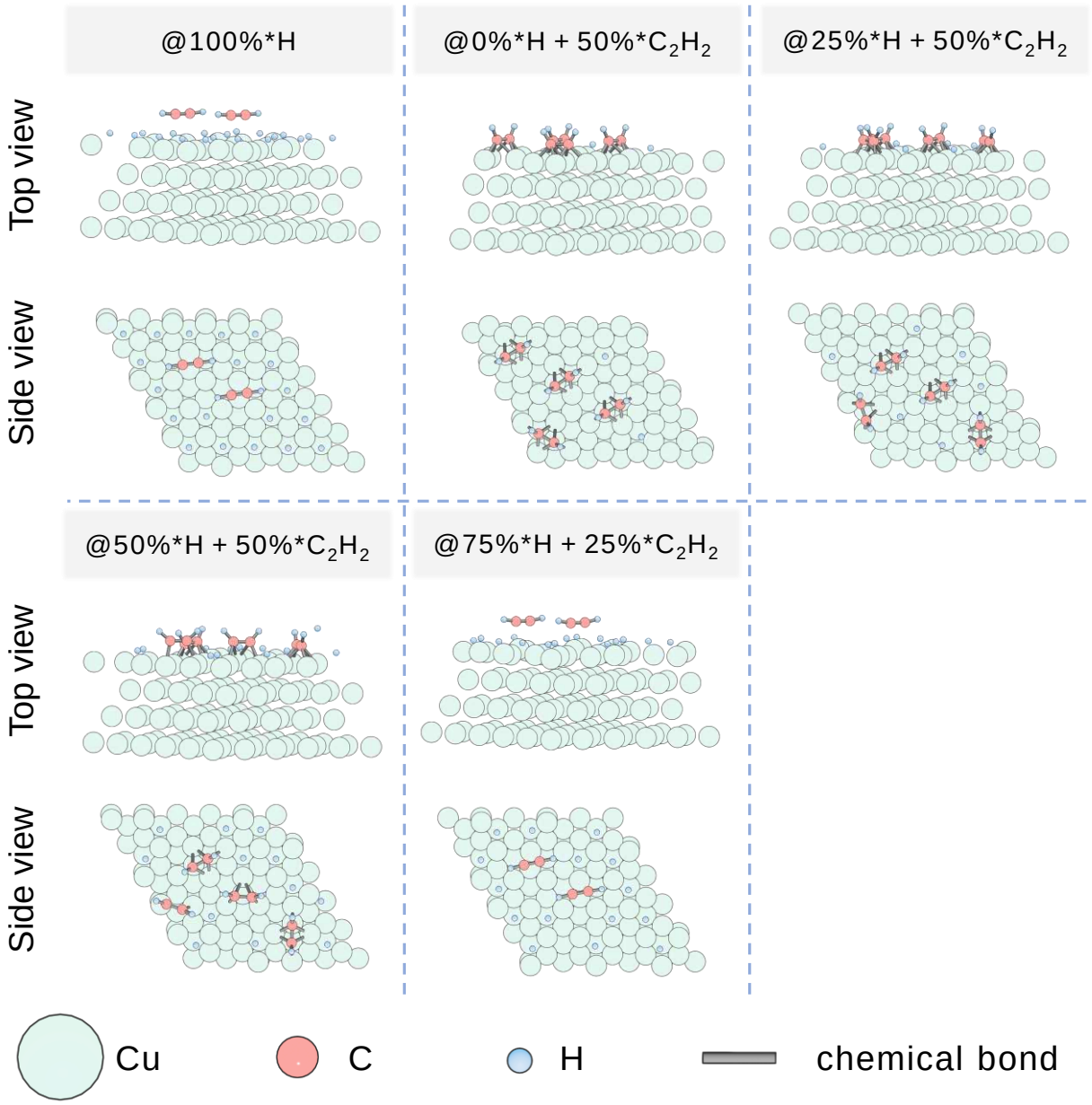

Supplementary Figure 11. The optimized structures for theoretical calculations. Theoretical adsorption models of the dimeric hydrogenation process of C_2H_2 over different coverages of $*C_2H_2$ and *H.

Considering that our proposed electrocatalytic process using H_2O as the hydrogen source is prone to lead to an H_2O-enriched interface, achieving C_2H_2-dominant conditions is quite difficult; thus, the maximum coverage of $*C_2H_2$ in our simulation is set to 50%. In addition, @100% *H and @0% *H + 50% $*C_2H_2$ are constructed by placing two C_2H_2 molecules or two H atoms on the surface with 100% *H or 50% $*C_2H_2$, respectively.

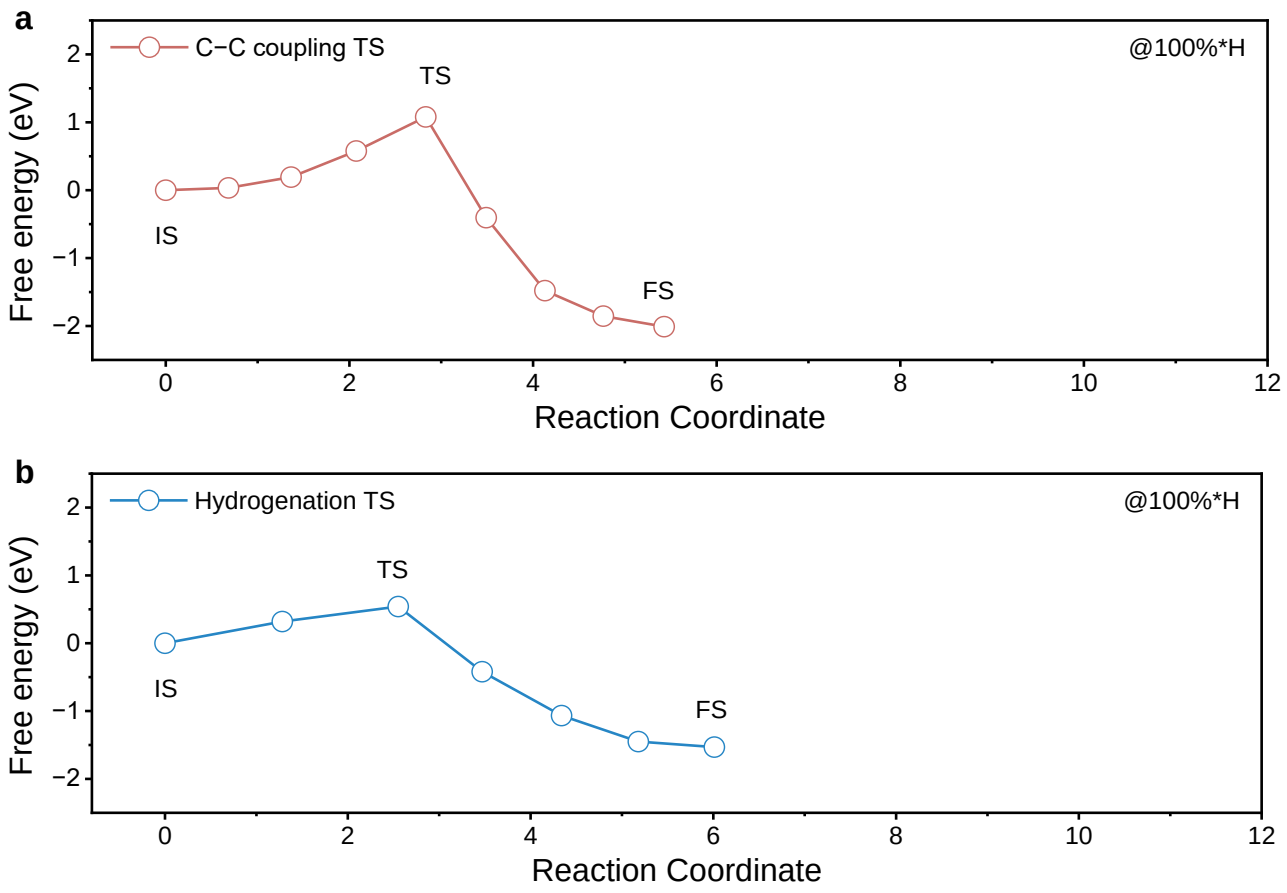

Supplementary Figure 12. Energy change profiles of the first step of the C_2H_2 dimeric hydrogenation process under 100% *H coverage.

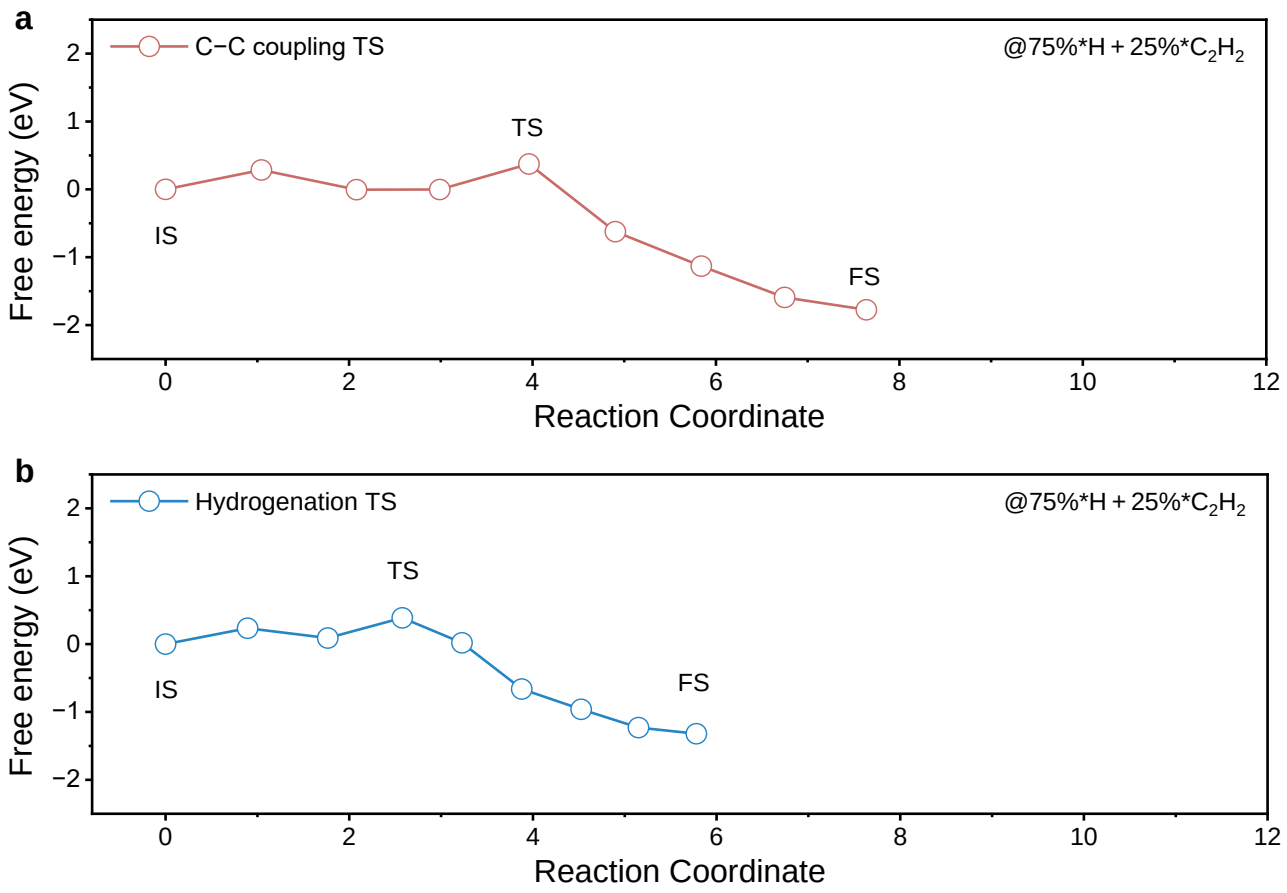

Supplementary Figure 13. Energy change profiles of the first-step reaction in the C_2H_2 dimeric hydrogenation process under 75% *H and 25% *C_2H_2 coverage.

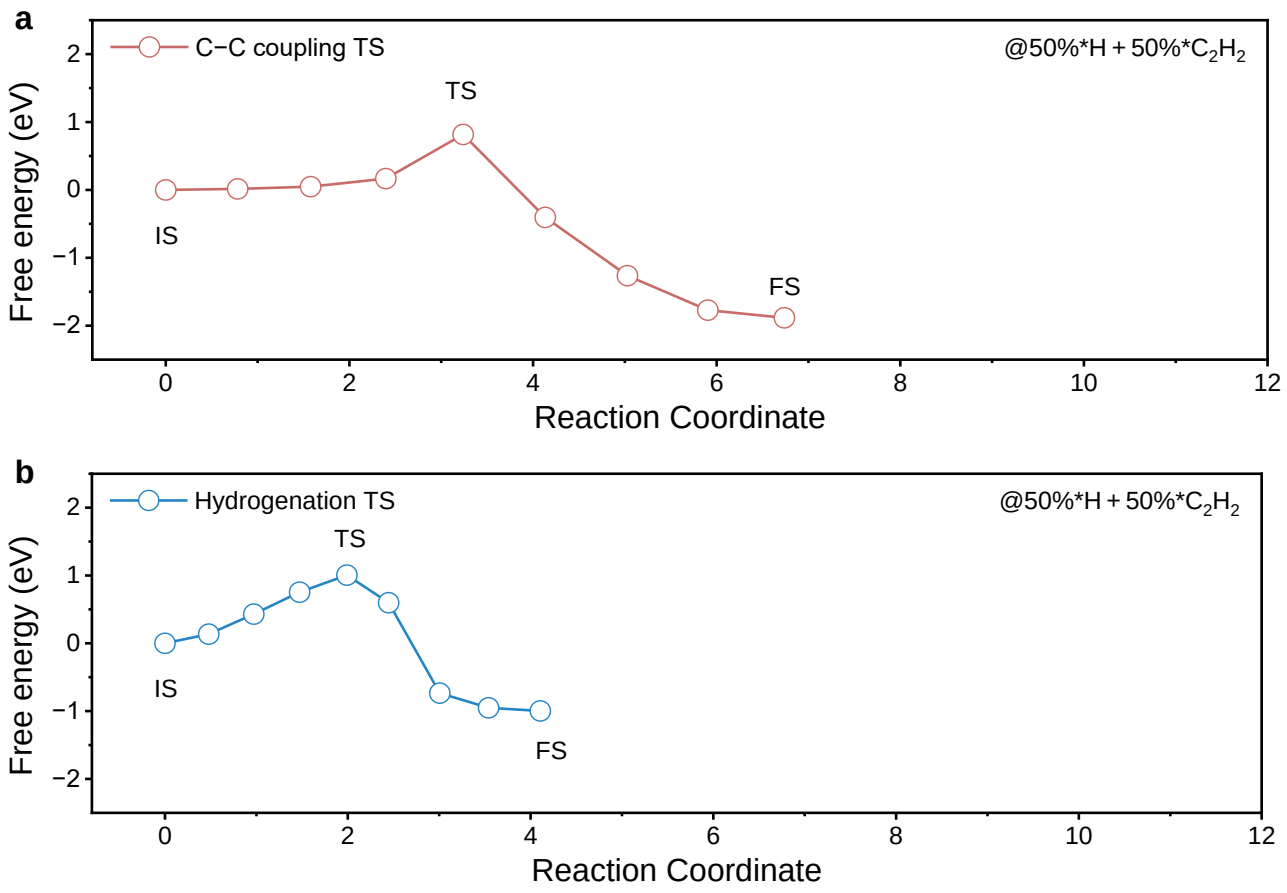

Supplementary Figure 14. Energy change profiles of the first-step reaction in the C_2H_2 dimeric hydrogenation process under 50% *H and 50% *C_2H_2 coverage.

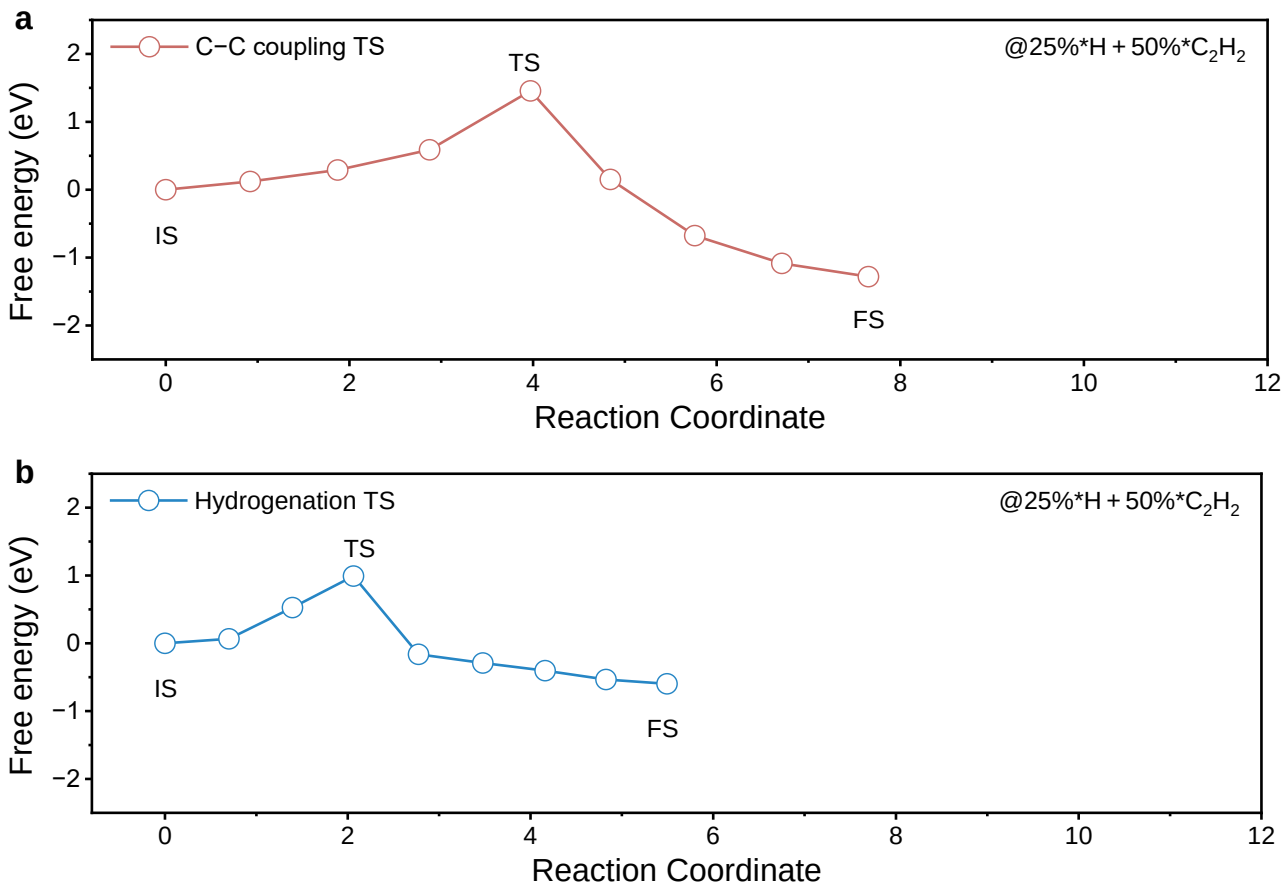

Supplementary Figure 15. Energy change profiles of the first-step reaction in the C_2H_2 dimeric hydrogenation process under 25% *H and 50% *C_2H_2 coverage.

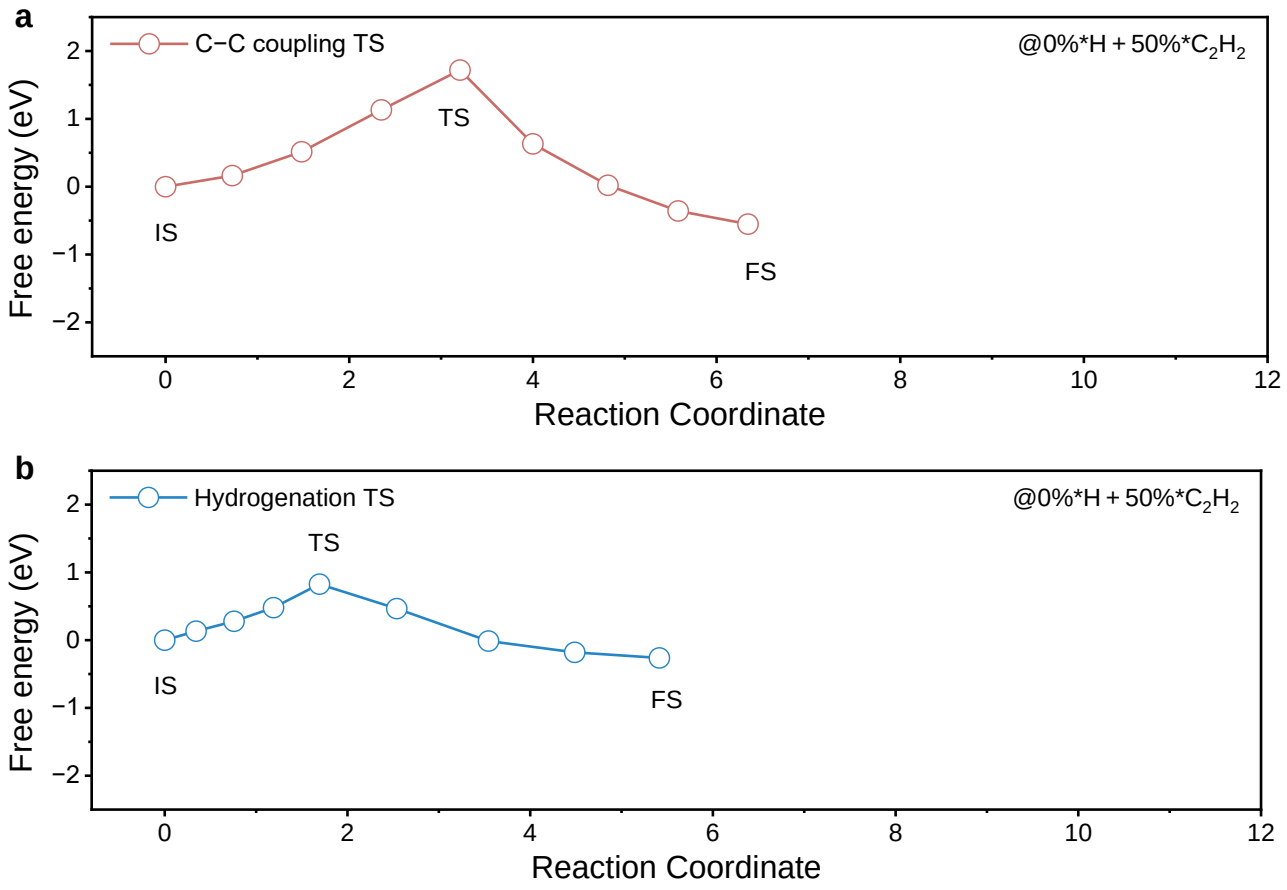

Supplementary Figure 16. Energy change profiles of the first-step reaction in the C_2H_2 dimeric hydrogenation process under 0% *H and 50% *C_2H_2 coverage.

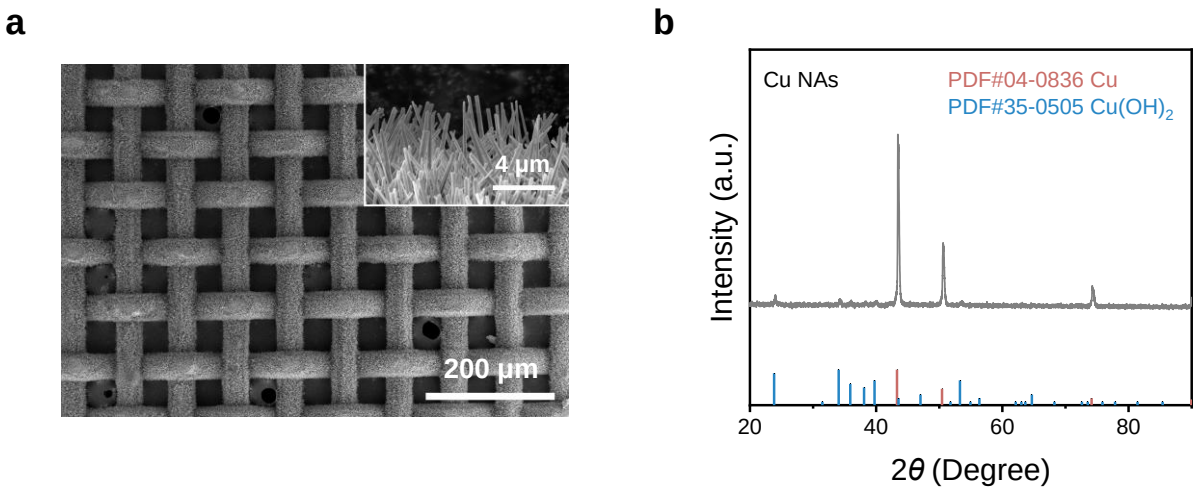

Supplementary Figure 17. SEM image and XRD pattern of the Cu NAs (insert: corresponding enlarged morphology).

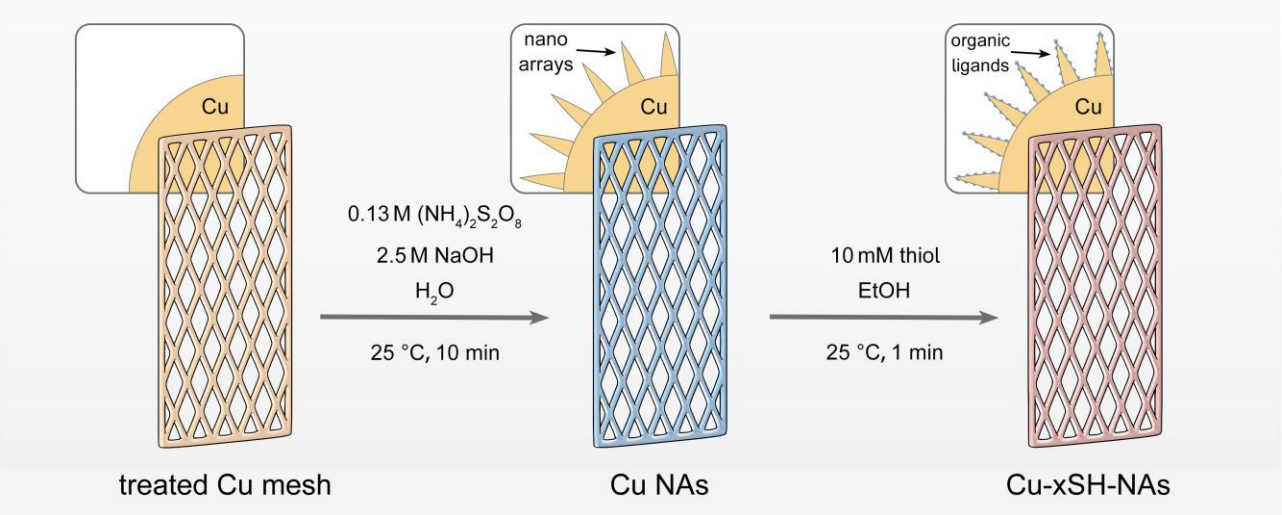

Supplementary Figure 18. Schematic illustration of the preparation of the Cu-xSH-NAs.

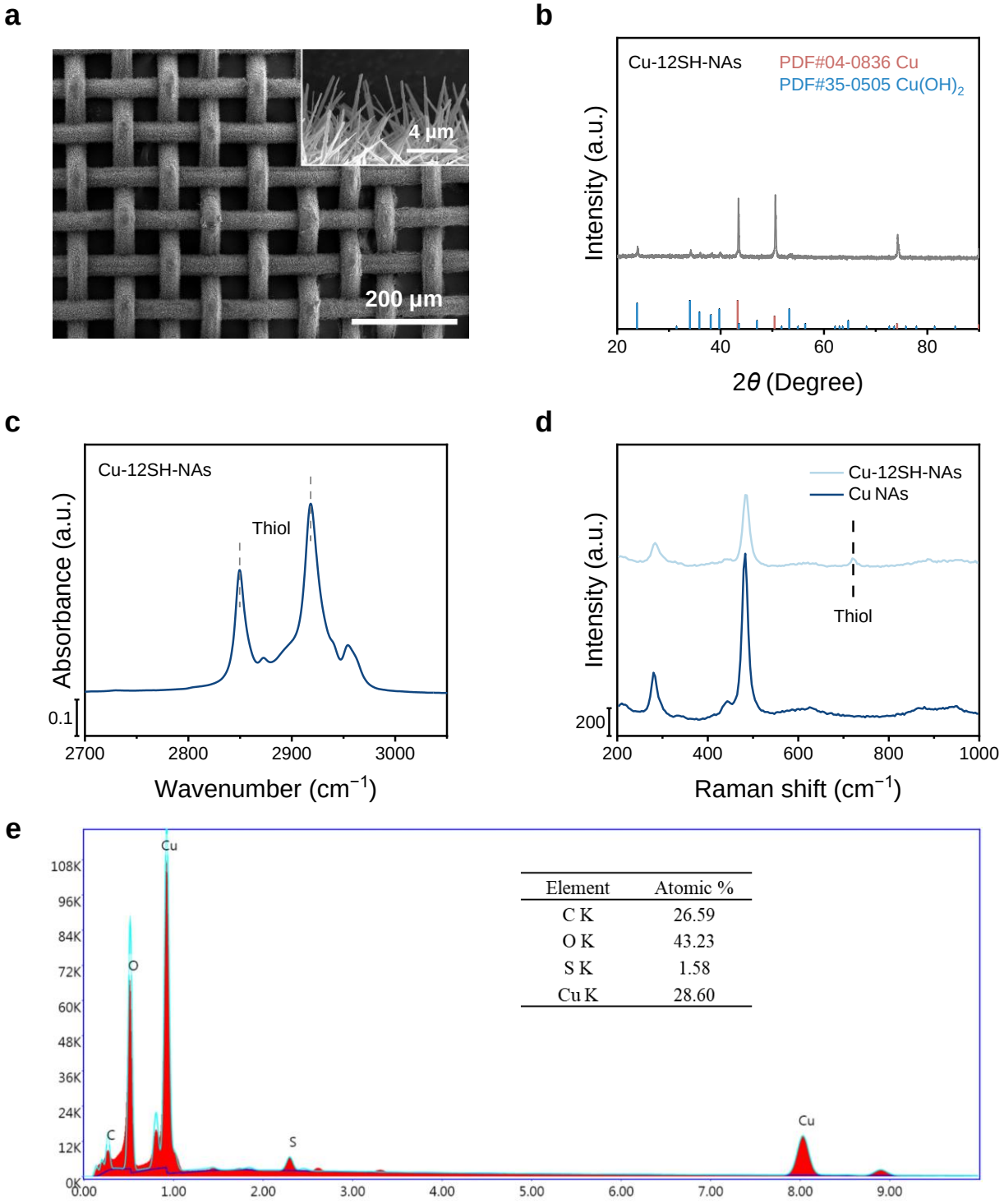

Supplementary Figure 19. SEM image (a), XRD pattern (b), FTIR spectra (c), Raman spectra (d), and EDS spectra (e) of the Cu-12SH-NAs (insert: corresponding enlarged morphology).

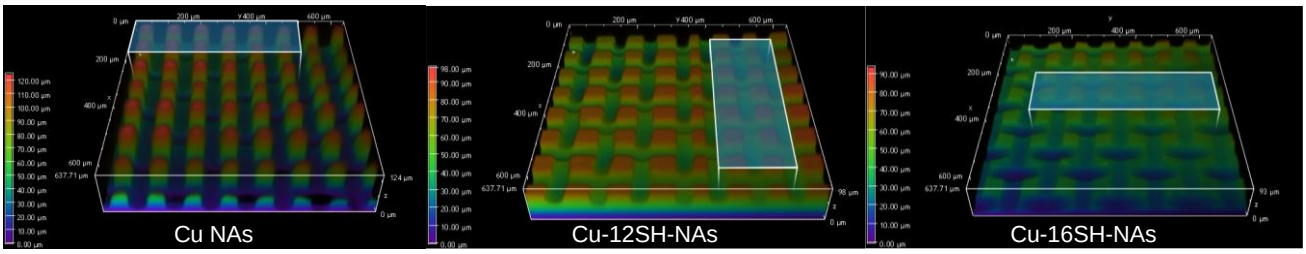

Supplementary Figure 20. Confocal 3D fluorescence intensity reconstruction images from the confocal laser scanning microscopy test (the slices correspond to the fluorescence intensity model in Fig. 2b).

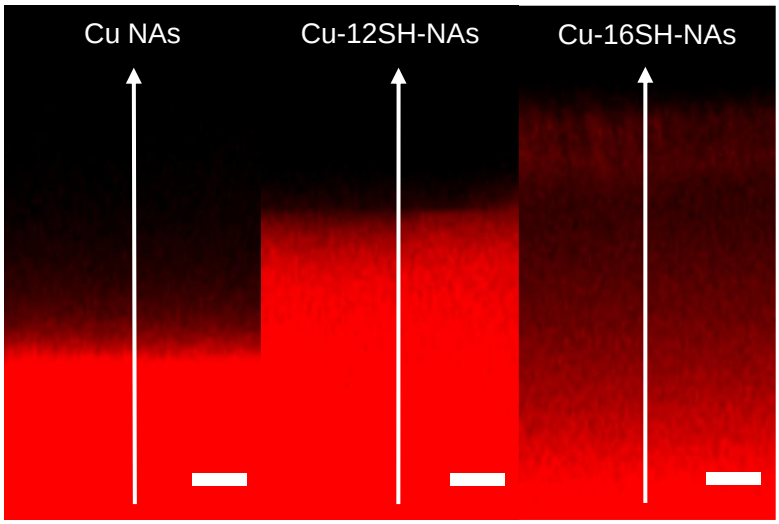

Supplementary Figure 21. Cross-sectional fluorescence images (scale bar: 10 μm) (white arrows correspond to the z-axis fluorescence intensity line scan in Fig. 2c).

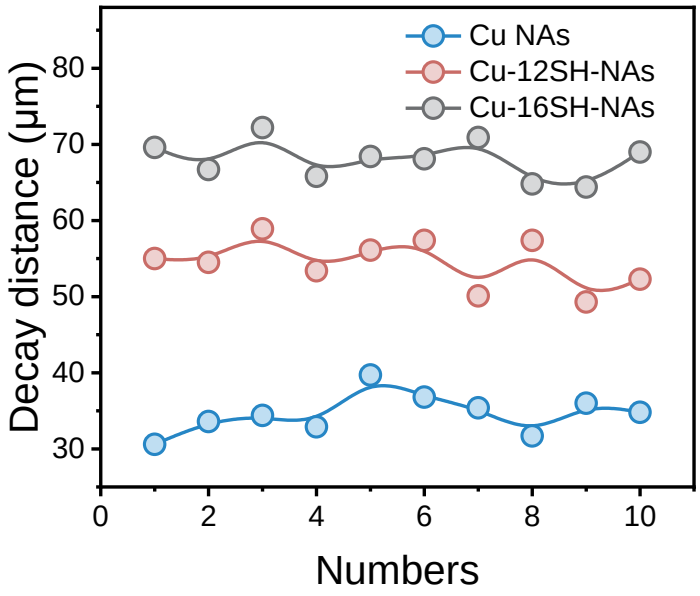

Supplementary Figure 22. Statistics of the fluorescence decay distance from the random area of the cross-sectional fluorescence images.

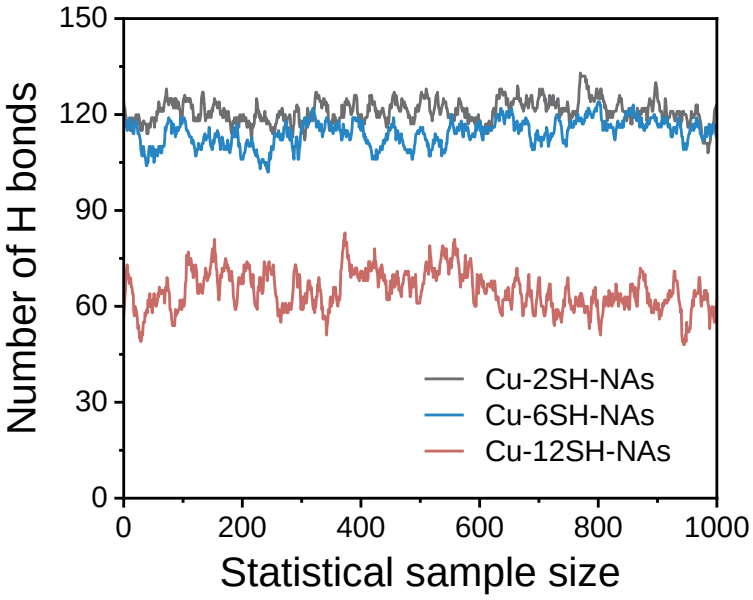

Supplementary Figure 23. The number of H bonds over the Cu-xSH-NAs (x = 2, 6, and 12).

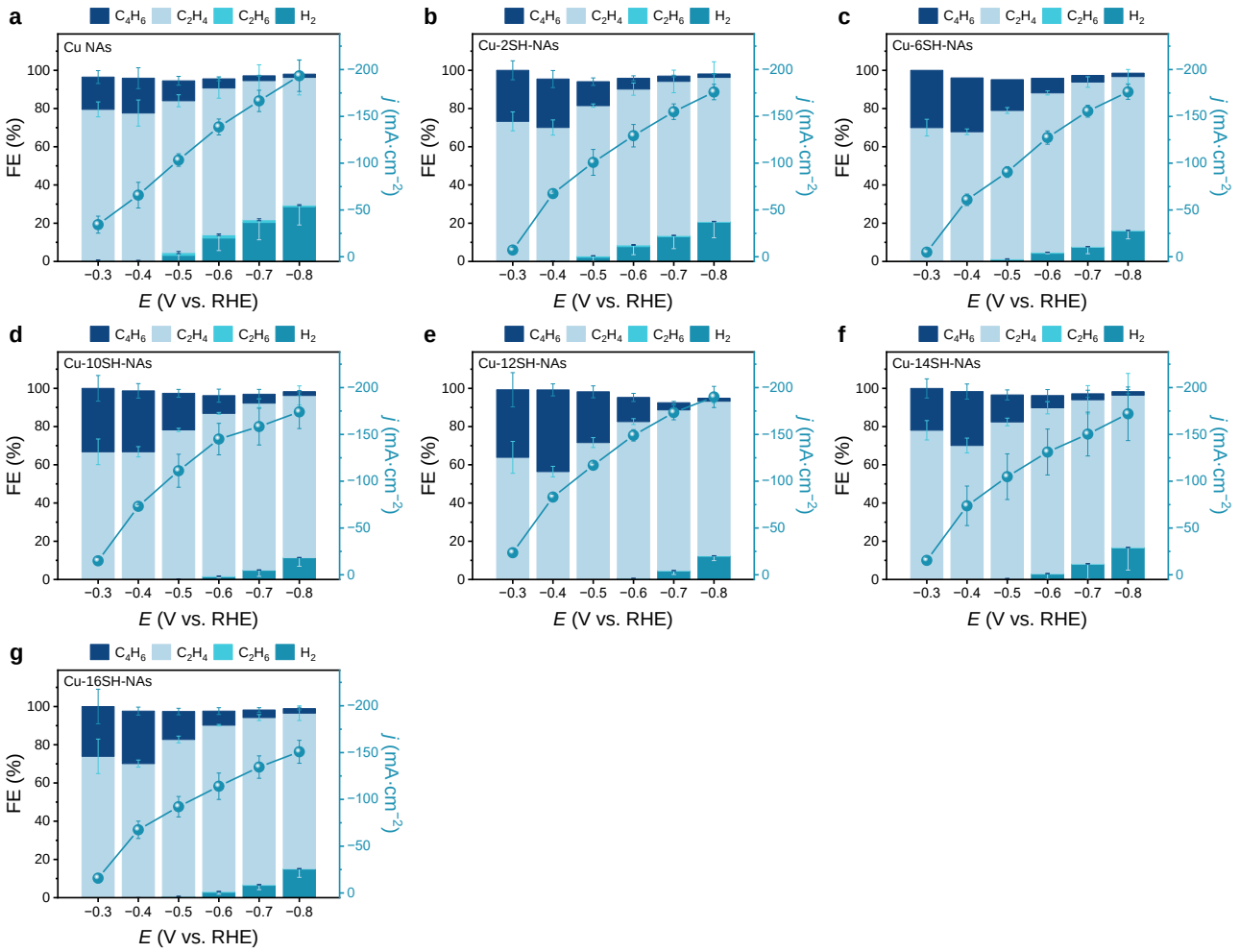

Supplementary Figure 24. FEs and current densities at different potentials in a 1 M KOH aqueous solution under 15% C_2H_2 flow over the Cu NAs and Cu-xSH-NAs. The error bars correspond to the standard deviation of at least three independent measurements.

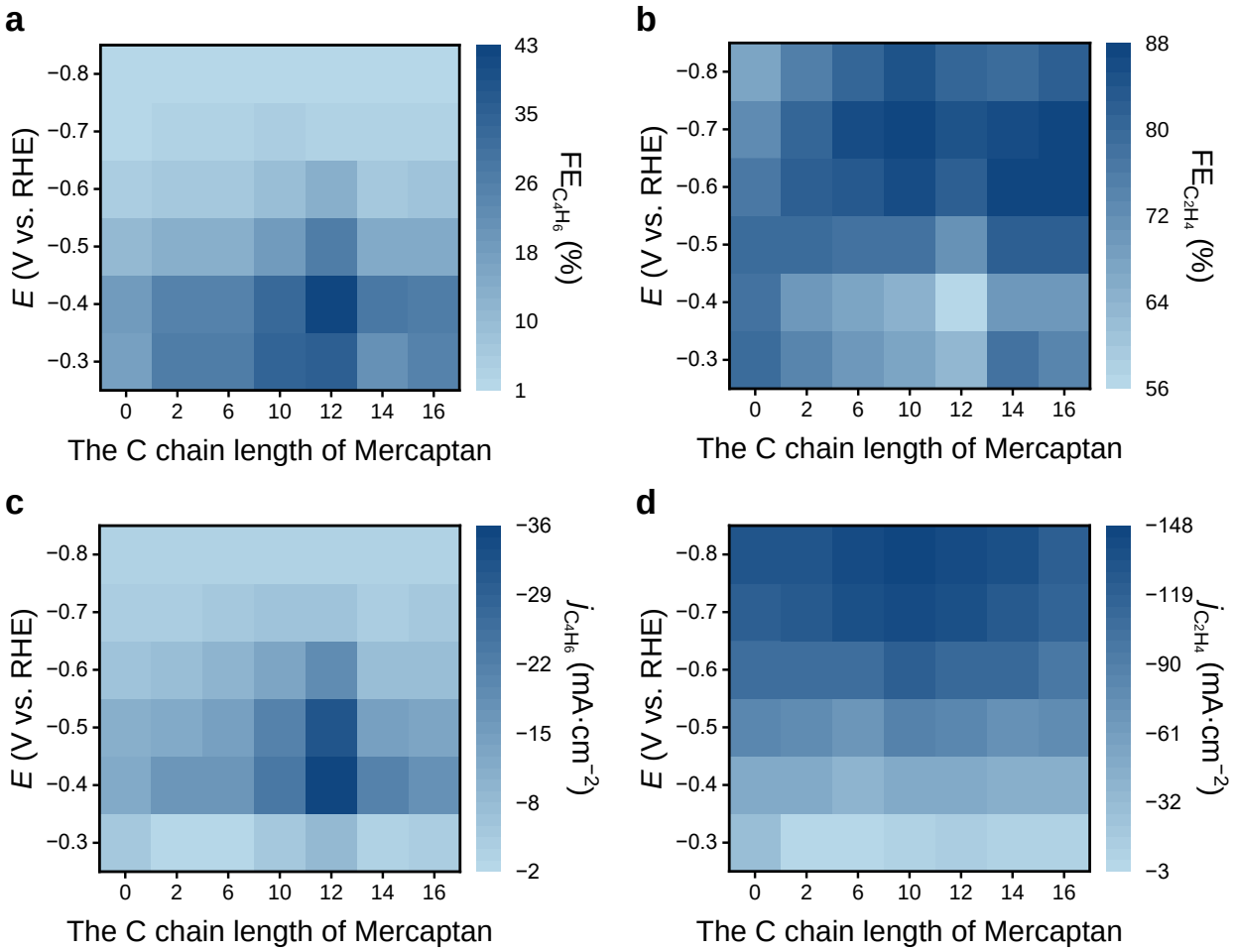

Supplementary Figure 25. (a, b) FEs and (c, d) partial current densities over the Cu NAs and Cu-xSH-NAs.

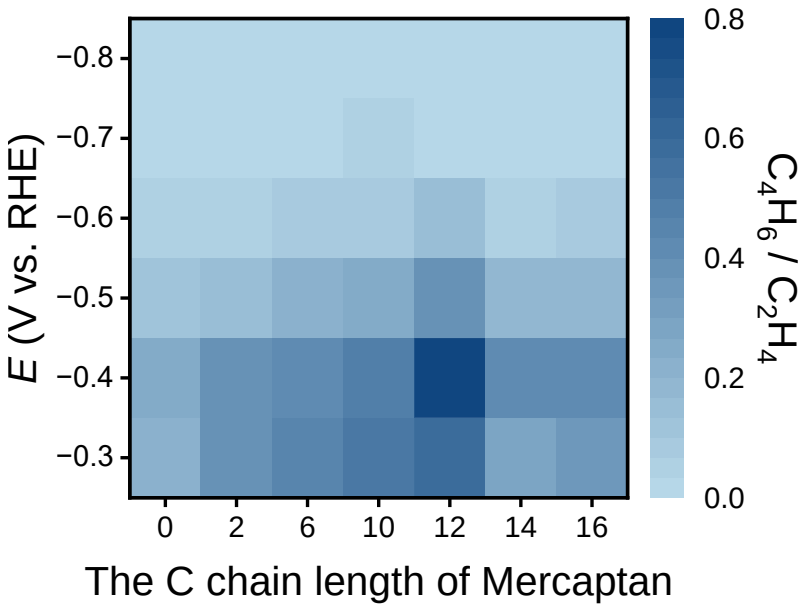

Supplementary Figure 26. FE ratios of C_4H_6 to C_2H_4 over the Cu NAs and Cu-xSH-NAs.

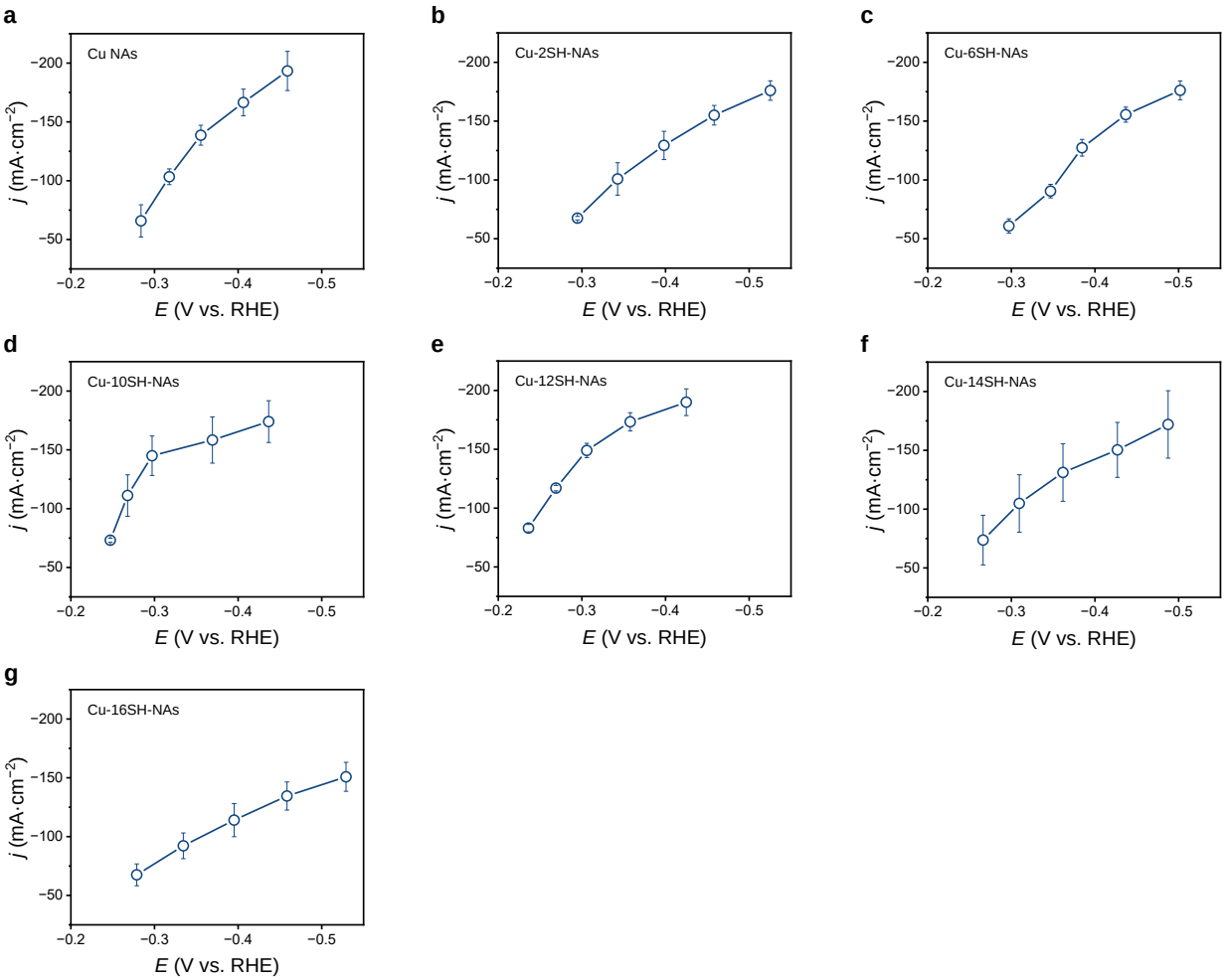

Supplementary Figure 27. Current densities after 80% *iR* compensation at different potentials in a 1 M KOH aqueous solution under 15% C_2H_2 flow over the Cu NAs and Cu-xSH-NAs, using for the following Tafel analysis. The error bars correspond to the standard deviation of at least three independent measurements.

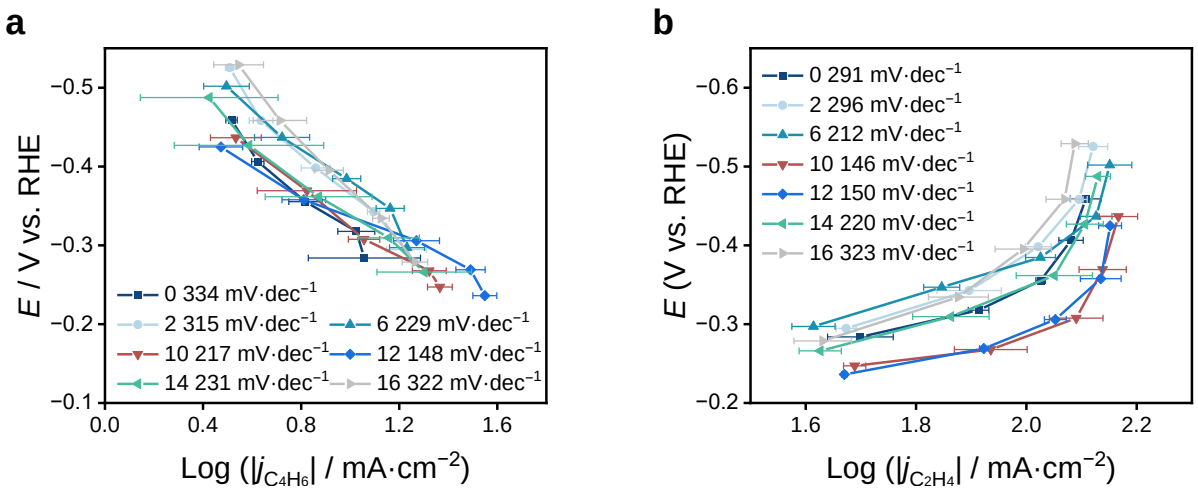

Supplementary Figure 28. Tafel analysis of C_4H_6 and C_2H_4. The error bars correspond to the standard deviation of at least three independent measurements.

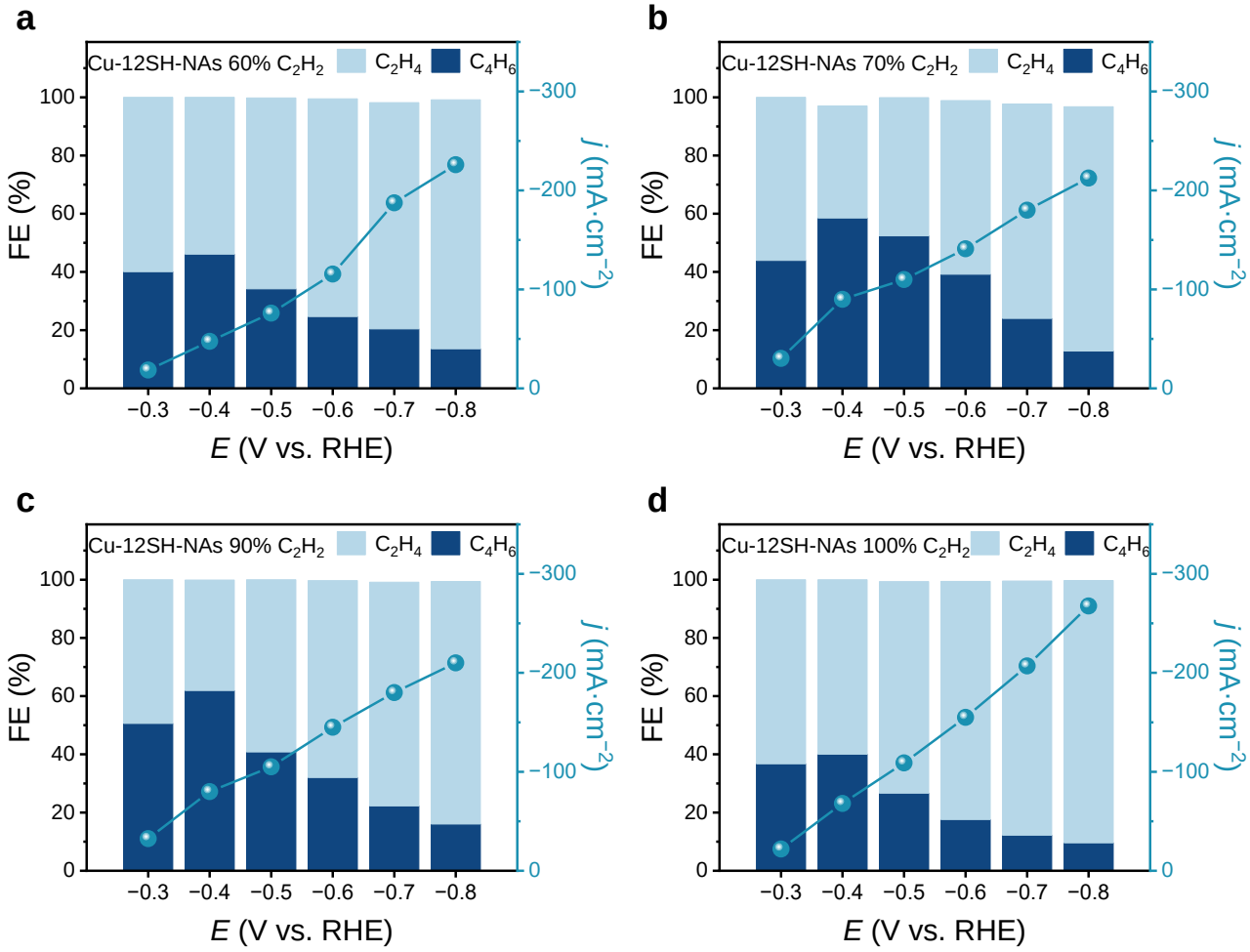

Supplementary Figure 29. FEs and current densities at different potentials in a 1 M KOH aqueous solution under different concentrations of C_2H_2 flow over the Cu-12SH-NAs.

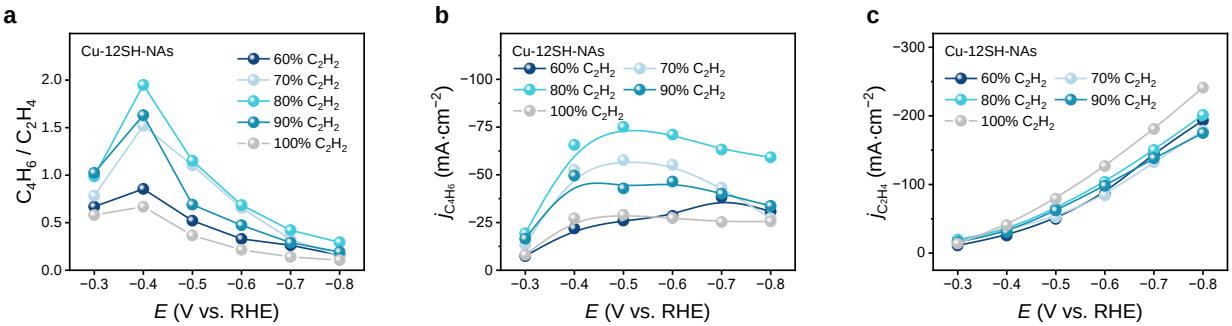

Supplementary Figure 30. FEs ratios of C_4 to C_2H_4 (a) and partial current densities (b, c) at different potentials in a 1 M KOH aqueous solution under different concentrations of C_2H_2 flow over the Cu-12SH-NAs.

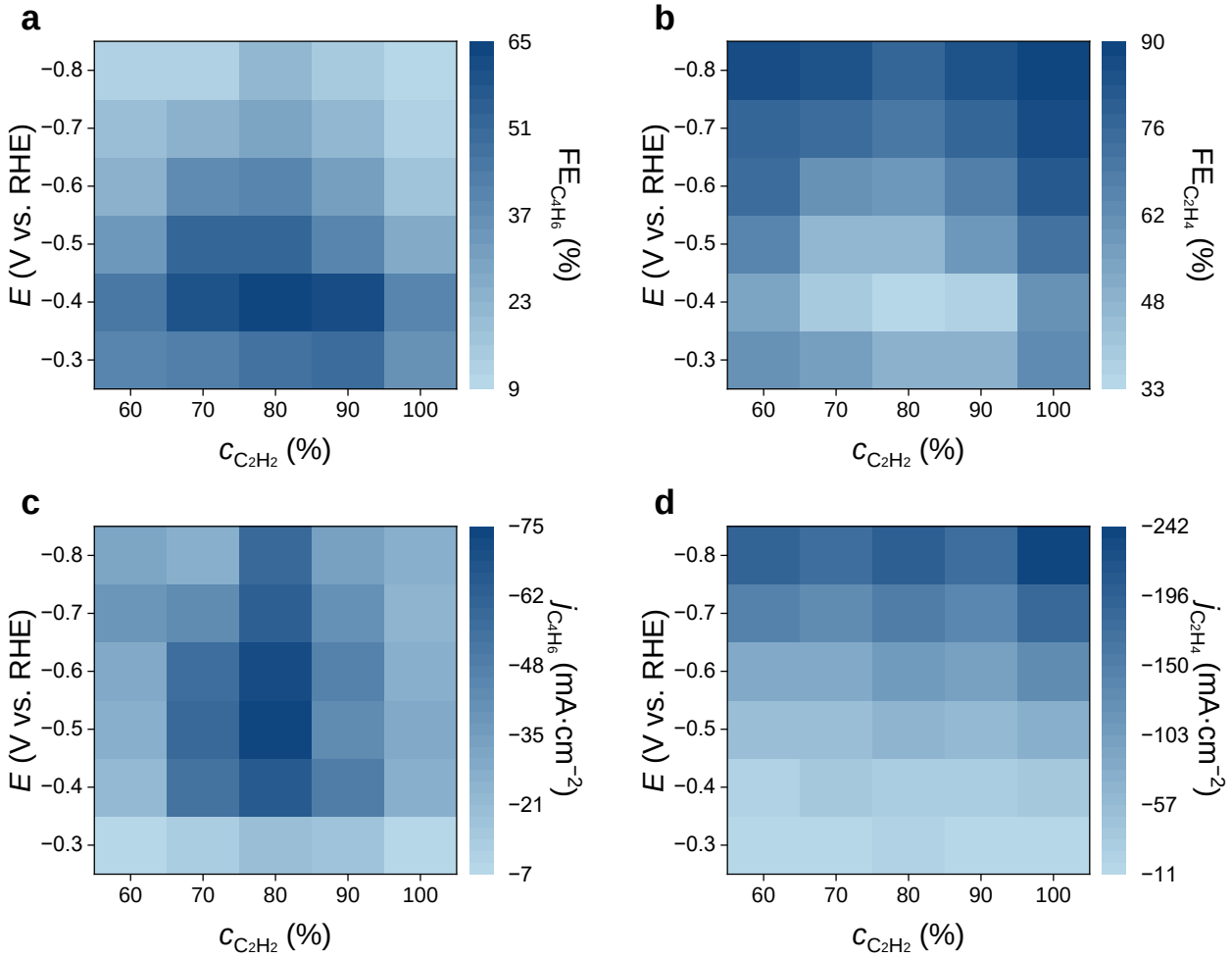

Supplementary Figure 31. FEs (a, b) and partial current densities (c, d) in a 1 M KOH aqueous solution under different concentrations of C_2H_2 flow over the Cu-12SH-NAs.

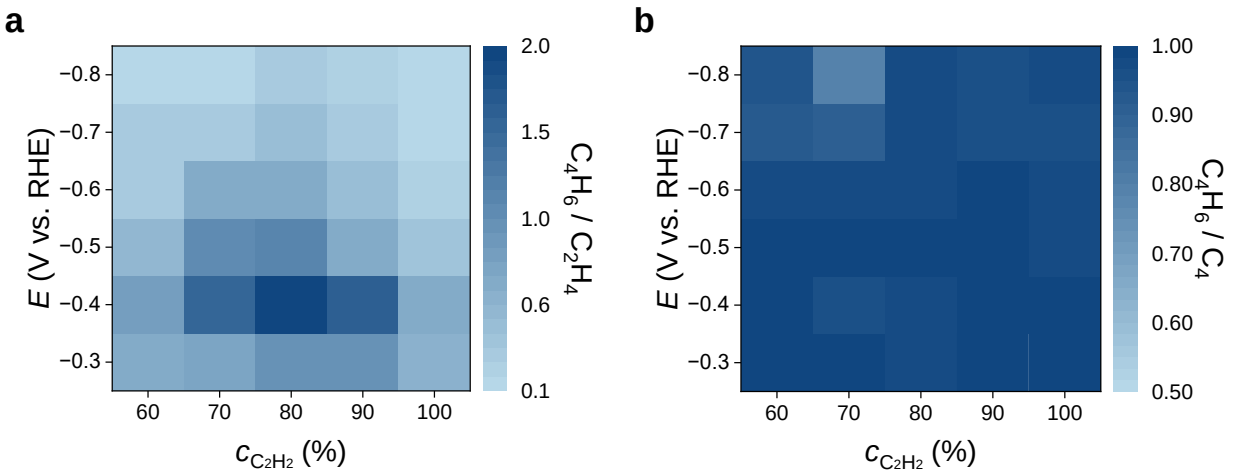

Supplementary Figure 32. FEs ratio of C_4H_6 to C_2H_4 (a) and the ratio of C_4H_6 to C_4 (b) in a 1 M KOH aqueous solution under different concentrations of C_2H_2 flow over the Cu-12SH-NAs.

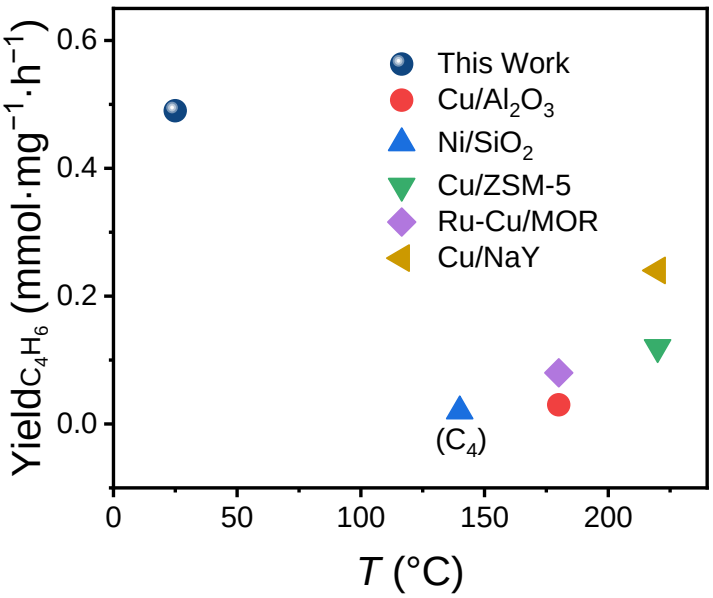

Supplementary Figure 33. Comparison of the yield of C_4H_6 at different temperatures of the Cu-12SH-NAs and the state-of-the-art reports (the details are shown in Supplementary Table 1).

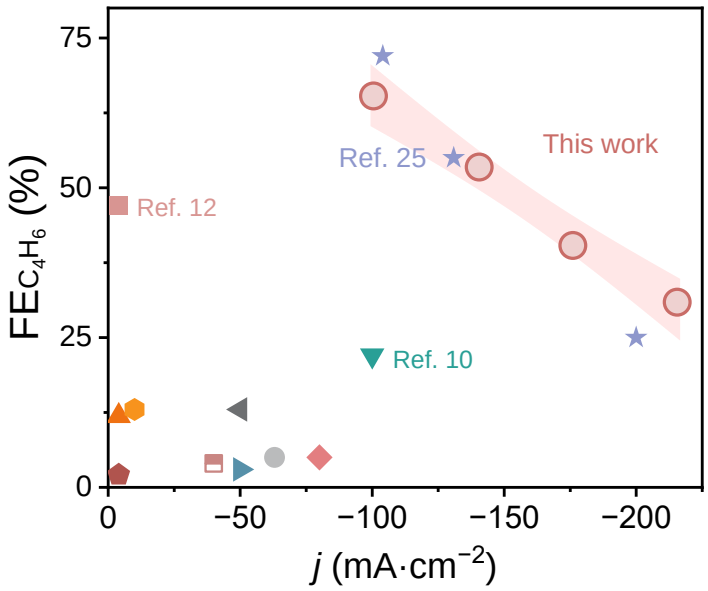

Supplementary Figure 34. Comparison of the FE and current density for C_4H_6 over different catalysts in the literature.

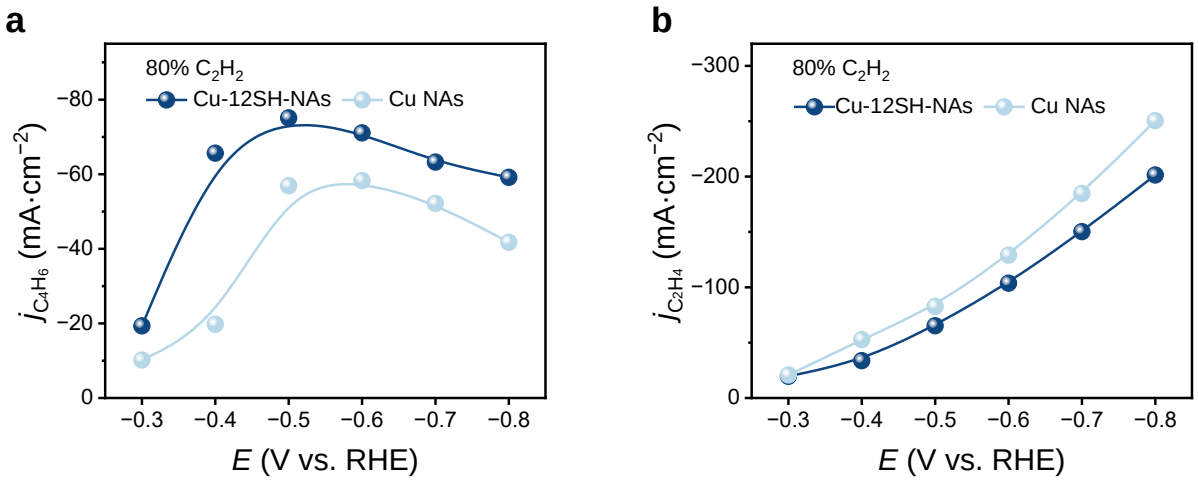

Supplementary Figure 35. Partial current densities at different potentials in a 1 M KOH aqueous solution under 80% C_2H_2 flow over the Cu-12SH-NAs and Cu NAs at different potentials.

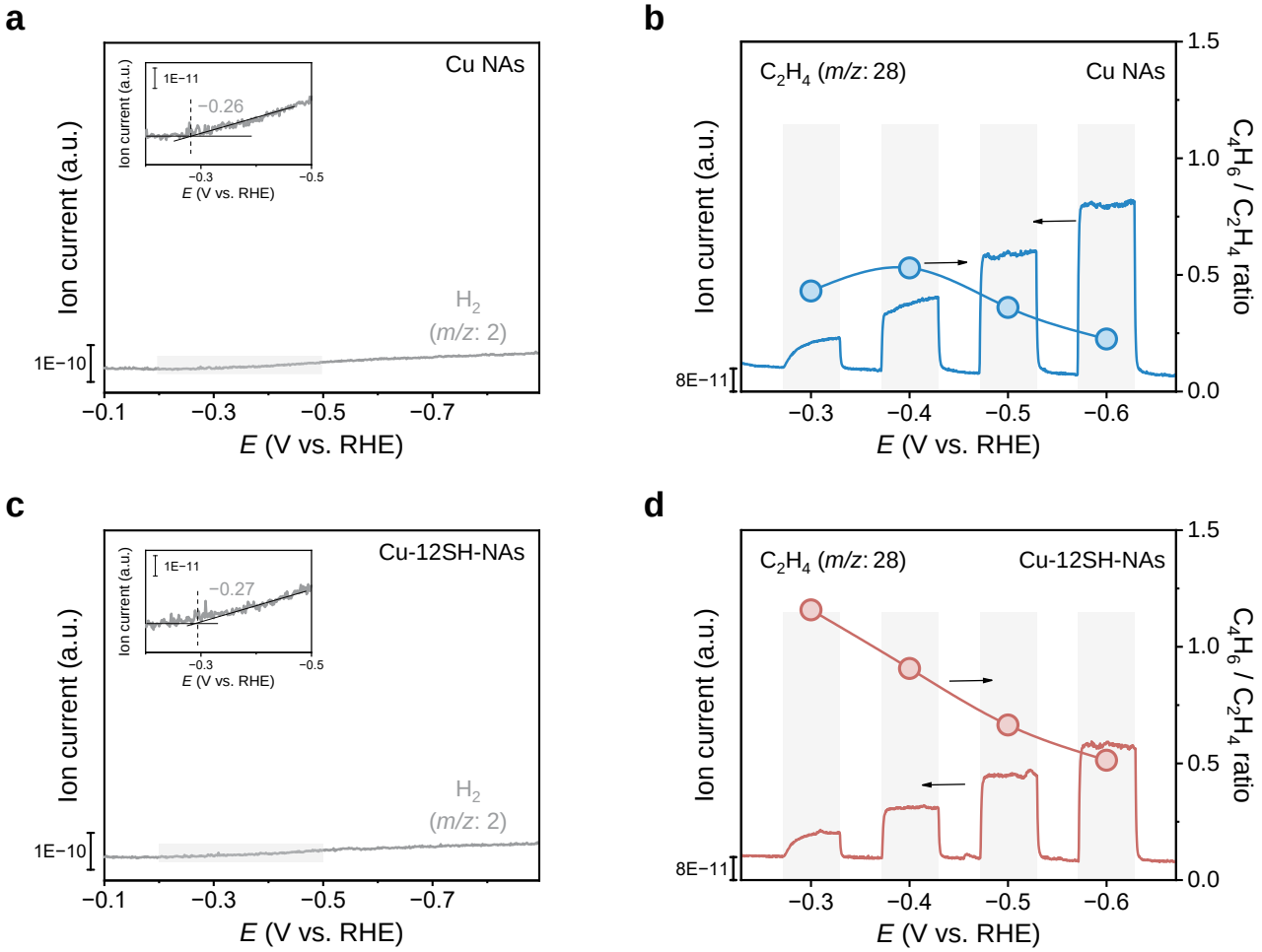

Supplementary Figure 36. Operando DEMS analysis of the Cu NAs (a, b) and Cu-12SH-NAs (c, d) in different modes.

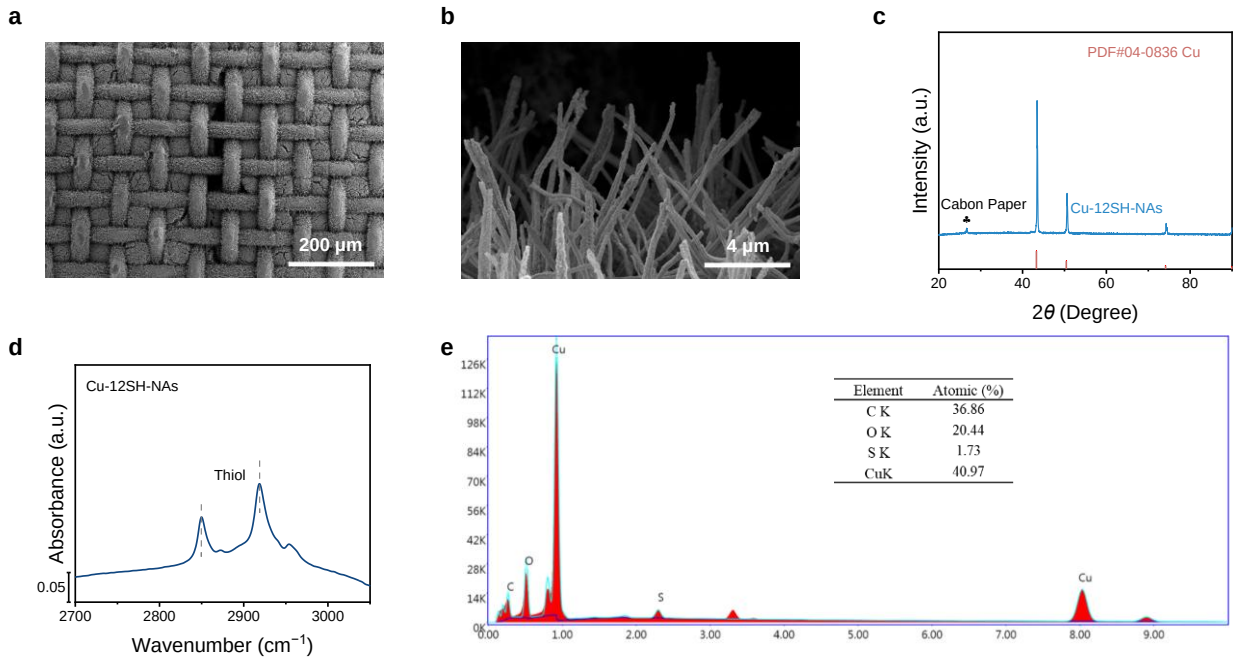

Supplementary Figure 37. SEM images (a, b), XRD pattern (c), FTIR spectra (d), and EDS spectra (e) of the Cu-12SH-NAs after the performance test.

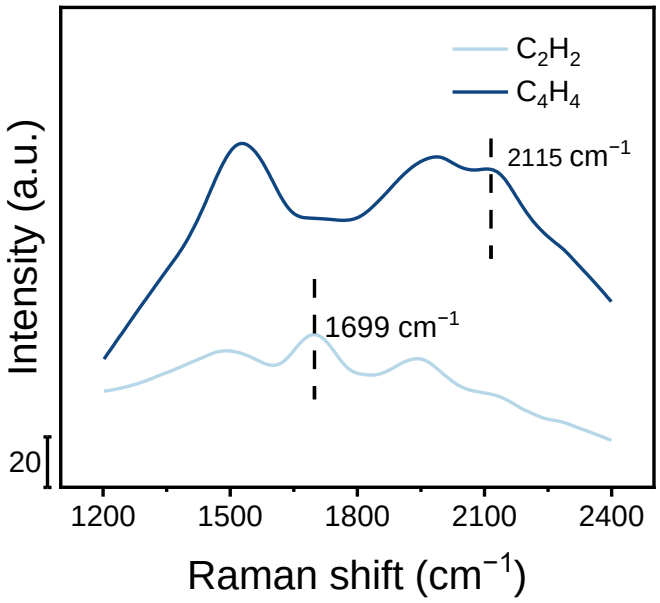

Supplementary Figure 38. Recognition of the characteristic Raman peaks of C_2H_2 and the reaction intermediate C_4H_4.

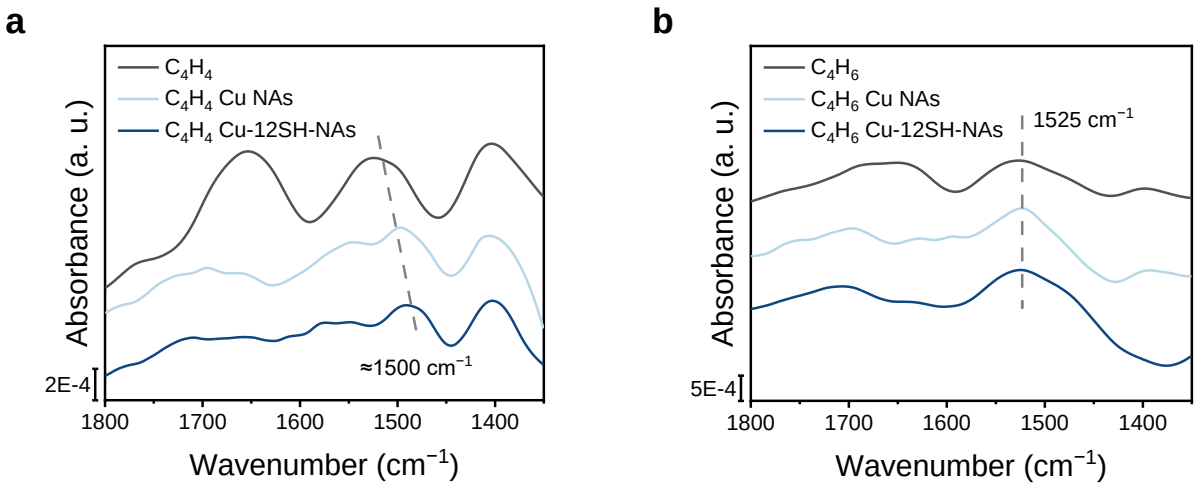

Supplementary Figure 39. Recognition of the characteristic FTIR peaks of the reaction intermediate C_4H_4 (a) and the product C_4H_6 (b).

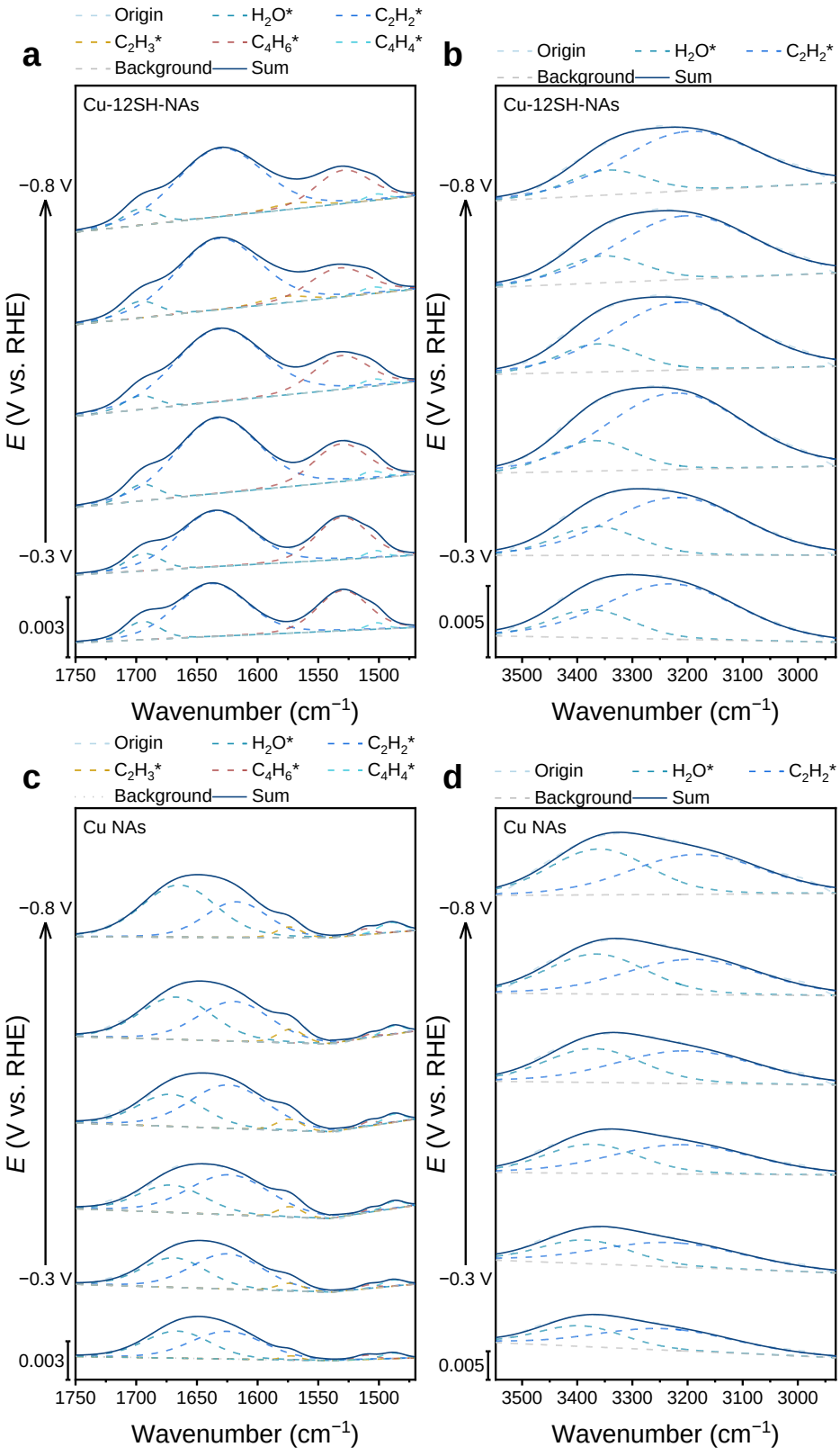

Supplementary Figure 40. Peak-differentiating and fitting analysis of the potential-dependent in situ ATR−FTIR data of the Cu-12SH-NAs (a, b) and Cu NAs (c, d) under a C_2H_2 atmosphere.

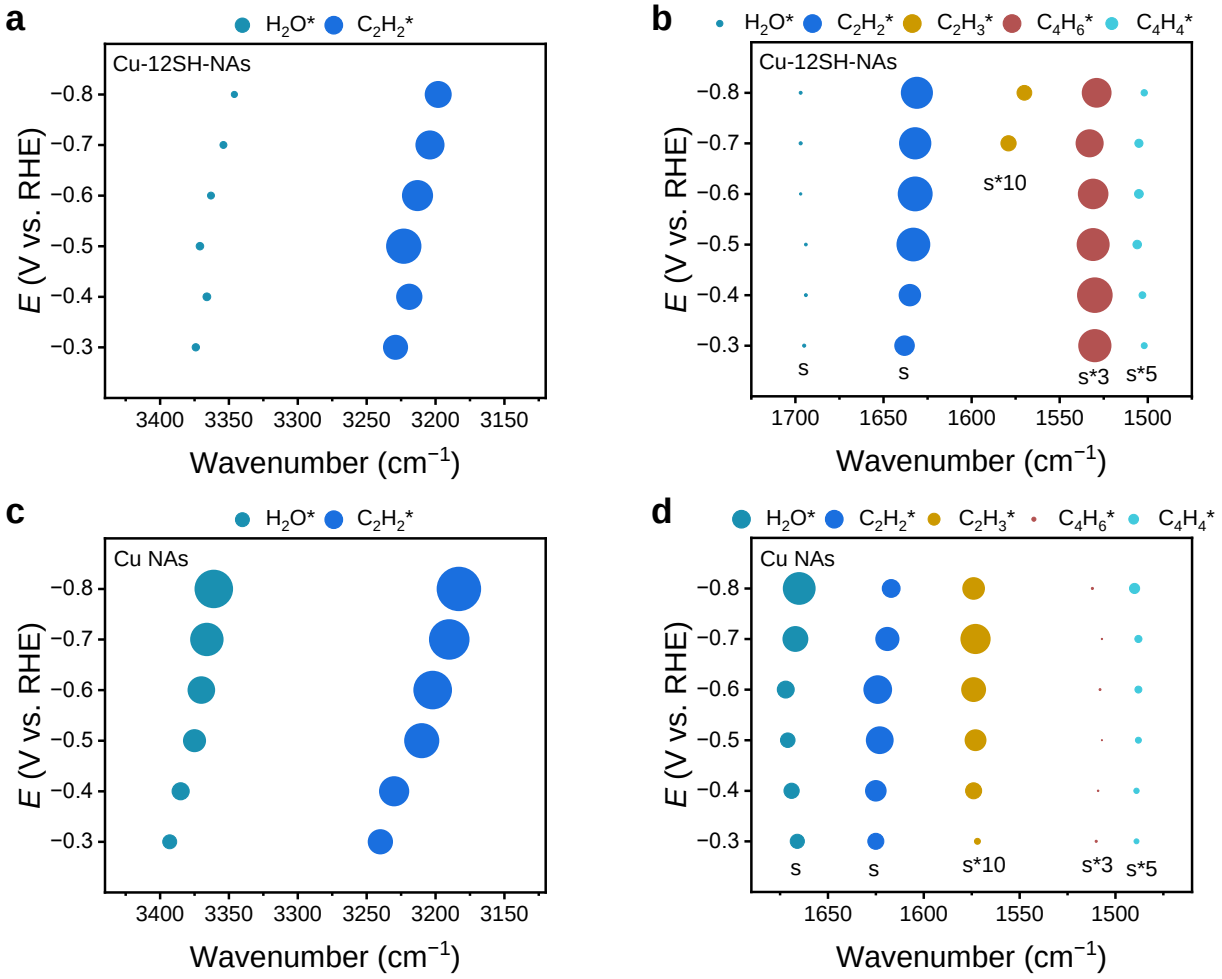

Supplementary Figure 41. Position and intensity of the characteristic peaks of potential-dependent in situ ATR−FTIR spectra of different species over the Cu-12SH-NAs (a, b) and Cu NAs (c, d).

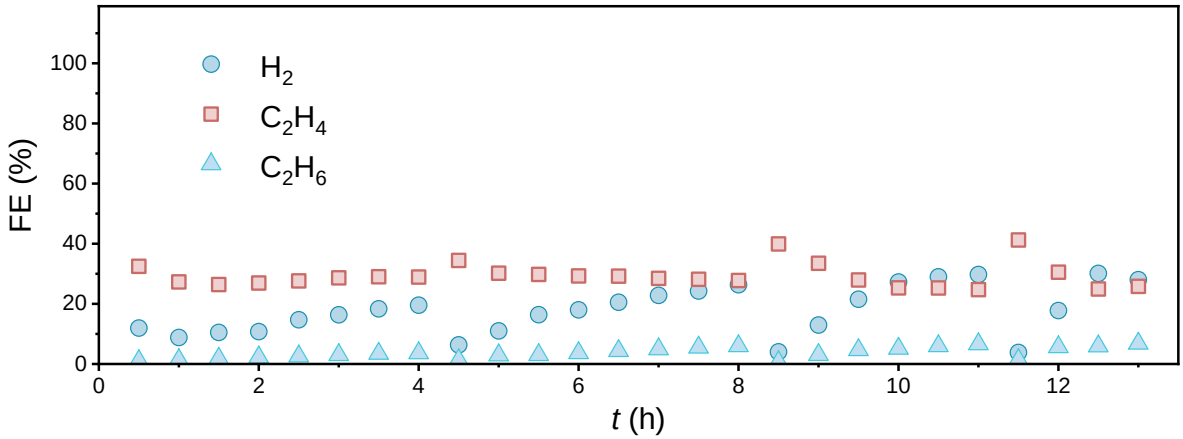

Supplementary Figure 42. Other products of the chronopotentiometry stability test of the Cu-12SH-NAs at a current of 1.0 A in the enlarged two-electrode reactor.

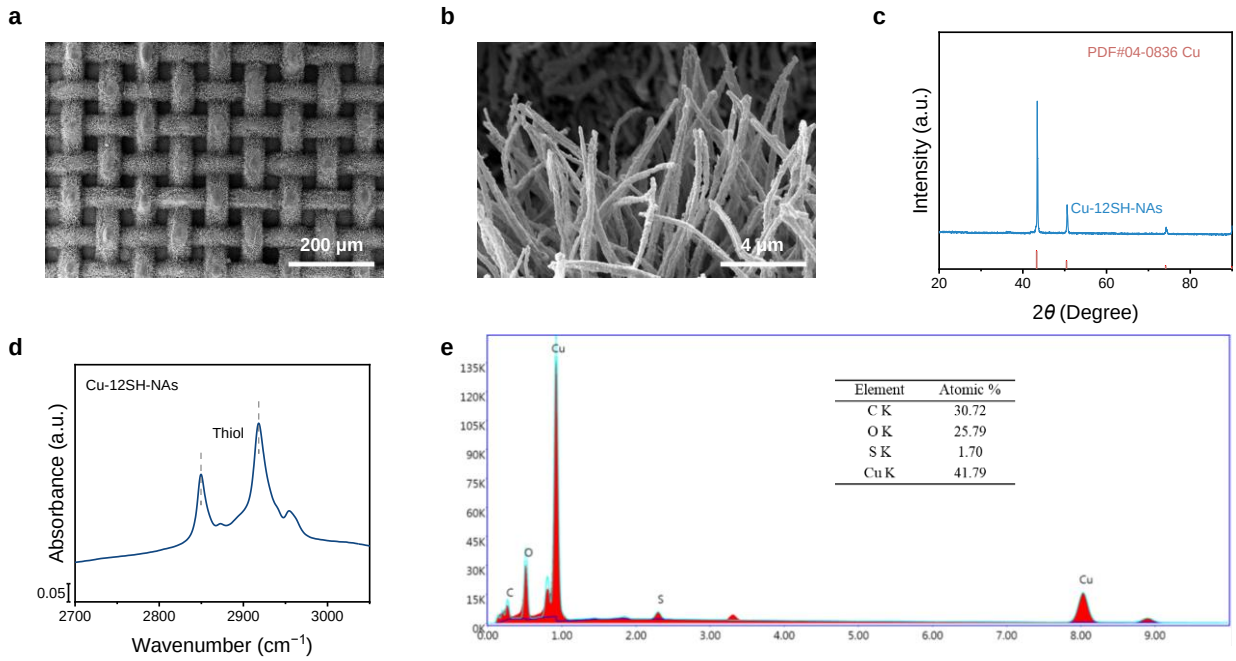

Supplementary Figure 43. SEM images (a, b), XRD pattern (c), FTIR spectra (d), and EDS spectra (e) of the Cu-12SH-NAs after the enlarged two-electrode test.

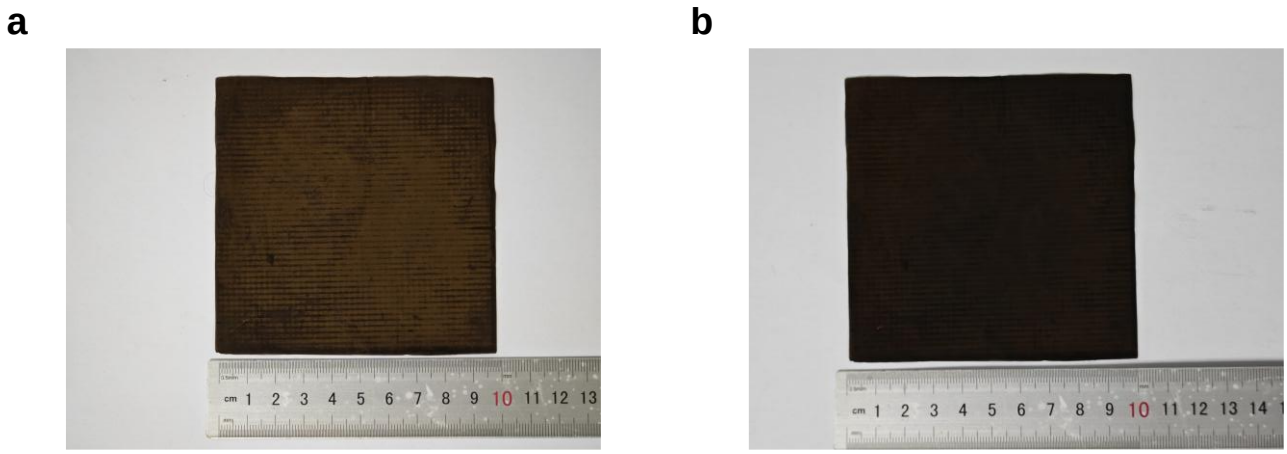

Supplementary Figure 44. Comparison of dry (a) and wet (b) cathode catalyst images.

5. Supplementary Tables

Supplementary Table 1. Comparison of the performance of the Cu-12SH-NAs and the state-of-the-art reports in the field of thermal catalysis.

Catalysts	$c_{C_2H_2}$ (%)	T (℃)	Selectivity$_{C_4H_6}$ (%)	Selectivity$_{C_4}$ (%)	SV (mL g^{-1} h^{-1})	Conversion (%)	Yield$_{C_4H_6}$ (mol g^{-1} h^{-1})	References
Cu-12SH-NAs	**80**	**25**	**65.7**	**66.3**	**/**	**25**	**0.49**	**This Work**
Cu/Al_2O_3	1	180	9.23	13	800000	100	0.03	*ACS Catal.***10**, 3495-3504 (2020)
Ni/SiO_2	25	140	/	13	15000	100	0.02 (C_4)	*J. Mol. Catal. A: Chem.* **288**, 63-74 (2008)
Cu/ZSM-5	20	220	55	74	36000	74	0.12	*ChemCatChem* **12**, 3321 (2020)
Ru-Cu/ MOR	25	180	75	/	36000	35	0.08	*ChemCatChem* **12**, 3321 (2020)
Cu/NaY	10	220	15	/	/	26S	0.24	*Ind. Eng. Chem. Res.* **62**, 1819-1825 (2023)
$Pd/\alpha\text{-}Al_2O_3$	55	25	23	/	/	20-30	/	*React. Kinet. Catal. Lett.* **74**, 299-307 (*20*01)
CuNPs@NU-907	50	200	/	45	/	85	/	*ACS Appl. Mater. Interfaces* **12**, 31496-31502 (2020)

Supplementary Table 2. Comparison of the performance of the Cu-12SH-NAs and the state-of-the-art reports in the field of electrocatalysis.

Catalysts	$c_{C_2H_2}$ (%)	Electrolyte	Potential	j (mA cm^{-2})	$FE_{C_4H_6}$ (%)	FE_{C_4} (%)	References
Cu-12SH-NAs	**80**	**1 M KOH**	**−0.4 V vs. RHE**	**−100.5**	**65.3**	**66.5**	**This Work**
Cu-12SH-NAs	**80**	**1 M KOH**	**−0.5 V vs. RHE**	**−140.5**	**53.5**	**53.6**	**This Work**
Cu-12SH-NAs	**80**	**1 M KOH**	**−0.6 V vs. RHE**	**−176**	**40.4**	**41.4**	**This Work**
Cu-12SH-NAs	**80**	**1 M KOH**	**−0.7 V vs. RHE**	**−215**	**30.9**	**30.9**	**This Work**
Cu dendrites	100	1 M KOH	−0.5 V vs. RHE	−63	/	5	*Nat. Catal.* **4**, 557-564 (2021)
LD-Cu	5	1 M KOH	−0.28 V vs. RHE	−4	/	11.9	*Nat. Catal.* **4**, 565-574 (2021)
Cu NDs	100	1 M KOH	−0.5 V vs. RHE	−100	/	22	*Nat. Commun.***14**, 2137 (2023)
2TIm	100	1 M KOH	−0.6 V vs. RHE	−80	/	5	*Nat. Chem.* **16**, 893-900 (2024)
Cu-F	70	1 M KOH	−0.4 V vs. RHE	−50	/	13	*Nat. Commun.* **14**, 8384 (2023)
$Cu_3(HITP)_2$	100	1 M KOH	−0.7 V vs. RHE	−50	/	3	*Small* 19, 2205845 (2023)
CuPc	100	1 M KOH	−0.4 V vs. RHE	−10	/	13	*Chem. Eng. J.* **431**, 134129 (2022)
NHC-Cu	100	1 M KOH	−0.6 V vs. RHE	−40	/	4	*Nat. Commun.* **12**, 6574 (2021)
Ag NWs	100	1 M KOH	−0.2 V vs. RHE	−4	2.1	/	*CCS Chem.* **5**, 200-208 (2023)
Cu MPs	100	1 M KOH	−0.3 V vs. RHE	−4	47	/	*Nat. Commun.* **12**, 7072 (2021)
Cu_2O_{NC}	100	1 M KI	−1.0 V vs. SHE	−104	72	/	*Nat. Catal.* DOI: 10.1038/s41929-024-01250-0 (2024)
Cu_2O_{NC}	100	1 M KI	−1.05 V vs. SHE	−136	55	/	*Nat. Catal.* DOI: 10.1038/s41929-024-01250-0 (2024)
Cu_2O_{NC}	100	1 M KI	−1.2 V vs. SHE	−200	25	/	*Nat. Catal.* DOI: 10.1038/s41929-024-01250-0 (2024)
Cu-DMF	0.45 mmol	DMF + 0.1 M $(C_3H_7)_4NBF_4$	−2.9 V vs. SCE	−2.3	34	/	*Electrochem. Commun.* **34**, 90-93 (2013)

Supplementary Table 3. Electrocatalytic C_2H_2 hydrogenation performance of the Cu-12SH-NAs in a 1 M KOH aqueous solution under 80% C_2H_2 flow.

Potential (V vs. RHE)	j (mA cm^{-2})	FE_{H_2} (%)	$FE_{C_2H_4}$ (%)	$FE_{C_2H_6}$ (%)	$FE_{C_4H_6}$ (%)	$FE_{1\text{-}C_4H_8}$ (%)	$FE_{(E)\text{-}2\text{-}C_4H_8}$ (%)	$FE_{(Z)\text{-}2\text{-}C_4H_8}$ (%)	C_4H_6/C_4 (%)
−0.3	39.5	n.d.	49.50	n.d.	48.94	0	1.52	0	96.99
−0.4	100.5	n.d.	33.50	n.d.	65.32	0.04	1.14	0	98.22
−0.5	140.5	n.d.	46.41	n.d.	53.46	0.04	0.09	0	99.76
−0.6	176	n.d.	58.89	n.d.	40.38	0.04	0.12	0.57	98.22
−0.7	215.5	n.d.	69.71	n.d.	29.35	0.05	0.34	0.56	96.87
−0.8	262.5	n.d.	76.73	n.d.	22.54	0.06	0.49	0.17	96.87

[n.d.] indicates that the corresponding product was not detected.

Supplementary Table 4. Constants for the carbon emissions life-cycle assessment.

Constants	Value	Unit
The energy intensity of C_4H_6	1.38[16]	kWh/kg C_2H_4
CO_2 emissions from the mining of coal	0.121	kg CO_2/kg Coal
CO_2 emission of reference C_4H_6 production	2.5	kg CO_2/kg C_2H_4
Energy for C_2H_4 separation	4.2	kWh/kg C_2H_4
Energy for C_2H_2 production	14	kWh/k gC_2H_2

6. Supplementary References

1 Huang, J. *et al.* Activating copper oxide for stable electrocatalytic ammonia oxidation reaction via in-situ introducing oxygen vacancies. *Nano Res.* **15**, 5987-5994 (2022).

2 Kresse, G. & Furthmüller, J. Efficient iterative schemes for ab initio total-energy calculations using a plane-wave basis set. *Phys. Rev. B* **54**, 11169-11186 (1996).

3 Blöchl, P. E. Projector augmented-wave method. *Phys. Rev. B* **50**, 17953-17979 (1994).

4 Perdew, J. P., Burke, K. & Ernzerhof, M. Generalized gradient approximation made simple. *Phys. Rev. Lett.* **77**, 3865-3868 (1996).

5 Mathew, K., Sundararaman, R., Letchworth-Weaver, K., Arias, T. A. & Hennig, R. G. Implicit solvation model for density-functional study of nanocrystal surfaces and reaction pathways. *J. Chem. Phys.* **140**, 084106 (2014).

6 Deng, W., Zhang, P., Seger, B. & Gong, J. Unraveling the rate-limiting step of two-electron transfer electrochemical reduction of carbon dioxide. *Nat. Commun.* **13**, 803 (2022).

7 Strmcnik, D. *et al.* Improving the hydrogen oxidation reaction rate by promotion of hydroxyl adsorption. *Nat. Chem.* **5**, 300-306 (2013).

8 Varela, A. S. *et al.* pH effects on the selectivity of the electrocatalytic CO_2 reduction on graphene-embedded Fe–N–C motifs: bridging concepts between molecular homogeneous and solid-state heterogeneous catalysis. *ACS Energy Lett.* **3**, 812-817 (2018).

9 Hellweg, S. & Milà i Canals, L. Emerging approaches, challenges and opportunities in life cycle assessment. *Science* **344**, 1109-1113 (2014).

10 Rojas Sánchez, D., Khalilpour, K. & Hoadley, A. F. A. How sustainable is CO_2 conversion to ethanol? – A life cycle assessment of a new electrocatalytic carbon utilisation process. *Sustain. Energy Fuels* **5**, 5866-5880 (2021).

11 Ma, J. *et al.* Pyrolysis of pulverized coal to acetylene in magnetically rotating hydrogen plasma reactor. *Fuel Process. Technol.* **167**, 721-729 (2017).

12 De Luna, P. *et al.* What would it take for renewably powered electrosynthesis to displace petrochemical processes? *Science* **364**, eaav3506 (2019).

13 Cabrera Camacho, C. E., Alonso-Fariñas, B., Villanueva Perales, A. L., Vidal-Barrero, F. & Ollero, P. Techno-economic and life-cycle assessment of one-step production of 1,3-butadiene from bioethanol using reaction data under industrial operating conditions. *ACS Sustain. Chem. Eng.* **8**, 10201-10211 (2020).

14 Wernet, G. *et al.* The ecoinvent database version 3 (part I): overview and methodology. *Int. J. Life Cycle Assess.* **21**, 1218-1230 (2016).

15 Yu, L. & Ren, Z. Systematic study of the influence of *iR* compensation on water electrolysis. *Mater. Today Phys.* **14**, 100253 (2020).

16 Mantingh, J. & Kiss, A. A. Enhanced process for energy efficient extraction of 1,3-butadiene from a crude C_4 cut. *Sep. Purif. Technol.* **267**, 118656 (2021).